Master thesis

Activity types in a neural mass model

Jurgen Hebbink

September 19, 2014

Exam committee:
Prof. Dr. S.A. van Gils (UT)
Dr. H.G.E. Meijer (UT)
Dr. G.J.M. Huiskamp (UMC Utrecht)

UNIVERSITY OF TWENTE.

Contents

Chapter 1

Introduction

Understanding neuronal activity in the human brain is a complex and difficult but necessary task in order to treat diseases like epilepsy. Due to the complexity there are multiple fields of science involved. One, at first glance surprising, way to study brain activity is by using mathematical models.

Mathematical models for brain activity are a useful tool because one can study brain activity without bothering about effects from outside. Experiments that one can do in a mathematical model are ideal in comparison to real experiments which are always performed under non-ideal conditions. Further one can change parameters in mathematical models easy, something that is difficult or even impossible in real experiments. A drawback of mathematical models is that they are always a simplification of the reality. However, a good mathematical model may give insight in the underlying processes that generates brain activity.

There are lots of different mathematical models for brain activity. All these models have their specific strength and weakness. Some of these models are made to model activity of single neurons. Often multiple of these single neuron models can be coupled in order to simulate a large network of neurons. However, one needs lots of coupled neurons to model bigger brain structures. For example a single cortical column counts in the order of 10^4-10^8 neurons [7].

Performing simulations of such large networks of coupled neurons is only feasible on supercomputers and even then it takes long. Another disadvantage of such big models is that they count a huge number of parameters. It's therefore difficult to analyze the influence of the parameters.

Other classes of mathematical models describe neuronal activity on a macroscopic level. These macroscopic models are less detailed then microscopic models and often describe average activity of a large group of neurons. This is not a big problem since most experimental data is the result of measurements of large groups of neurons. This is for example the case with EEG measurements.

An advantage of macroscopic models is that they need less computation time compared to microscopic ones. Simulations of macroscopic models can be done on a consumer PC. Further they have significantly less parameters and are therefore easier to analyze. Hence, studying macroscopic models may give more insight in brain activity.

In this report we will study a class of macroscopic models that is called Neural Mass Models (NMMs). The basis of NMMs is formed in the seventies by Lopes da Silva et al. [20, 21] and by Freeman et al. [9]. In this report we will study a model by Wendling et al. [28] that models the behaviour of a cortical column. A feature of this model for a cortical column is that it models two different inhibitory processes, a fast and slow one. Most neural mass models for cortical columns model only the slow inhibitory process.

The main target of this report will be to investigate the different type of activities that this model can generate and what the influence of the two inhibitory processes is on these activity types. Another target is to find boundaries between the different activity types we find in this

model. This will result in a map that reveals regions where specific activity types are seen.

This report is built up in the following way. In the next chapter we start to explain the basic principle of a neural mass models. After this we give a literature overview of some neural mass models for cortical columns. In the chapter that follows we investigate the Wendling model in more detail. First we will formulate a system of differential equations that governs this model. Then we show the different activity types that can be produced by the Wendling model. This is followed by bifurcation analysis of the model in one parameter. The bifurcations we find give a part of the boundaries between the activity types. After this we will search how the other boundaries can be found. It results in an activity map and a bifurcation diagram for a large parameter region. Finally we will discuss our results in the chapter 'Conclusion & Discussion'.

To this report two appendices are added. In the first appendix is described how the non-bifurcation boundaries between the activity types can be continued using an extended system of differential equations. The last appendix shows the source code of our implementation of the Wendling model in Matlab.

Chapter 2

Neural mass models

In this chapter we will discuss neural mass models in more detail. The basic units of neural mass models are neural masses. A neural mass models the average behaviour of a large group of neurons. Neural masses are coupled together to model larger structures of neurons like cortical columns. Some neural mass models consist of multiple cortical columns that are coupled together.

In this chapter we describe first the general principle of neural mass models and explain how a single neural mass is modeled. Then we discuss one of the first neural mass model namely that of Lopes da Silva et al. [20]. We finish to comment on some literature on neural mass models for cortical columns.

2.1 General principle of a neural mass

In this section is described how a single neural mass or neural population is modeled. Each neural mass has average membrane potential, u. This average membrane potential can be viewed as the state variable of the neural mass. This average membrane potential is the result of the different inputs that this neural mass receives.

In neural mass models these inputs represents average pulse densities. These inputs can come from other neural masses in the model or from external inputs. A neural mass it self can also give an output. This output is also an average pulse density.

Average membrane potential and average pulse densities are the two main quantities in neural mass models. These two quantities are converted via two transformations: Post Synaptic Potential (PSP) and a potential-to-rate function. Each input to a neural mass is converted from an average pulse density to a potential via a PSP transform. Each of these potentials is multiplied by some constant, modeling the average number of synapses to this population. Then the average membrane potential of a population, u, is formed by summing up all potentials from excitatory inputs and subtract all inhibitory ones. The potential-to-rate function converts the average membrane potential of a neural mass into the average pulse density that this population puts out. A schematic overview of a neuronal population is displayed in figure 2.1.

The PSP transformation is a linear transformation and is modeled using a second order differential equation. This second order differential equation is usually characterized in terms of it's impulse response. Originally Lopes da Silva et al. [20] approximated the impulse response of a real PSP by the following impulse response:

$$h(t) = Q \left(e^{-q_1 t} - e^{-q_2 t} \right).$$

Here Q (in mV) and $q_1 < q_2$ (both in Hz) are parameters.

Van Rotterdam et al. [27] simplified this approximation by a version that has two parameters, Q and q. This impulse response is given by:

$$h(t) = \begin{cases} Qqte^{-qt} & t \geq 0 \\ 0 & t < 0 \end{cases}. \tag{2.1}$$
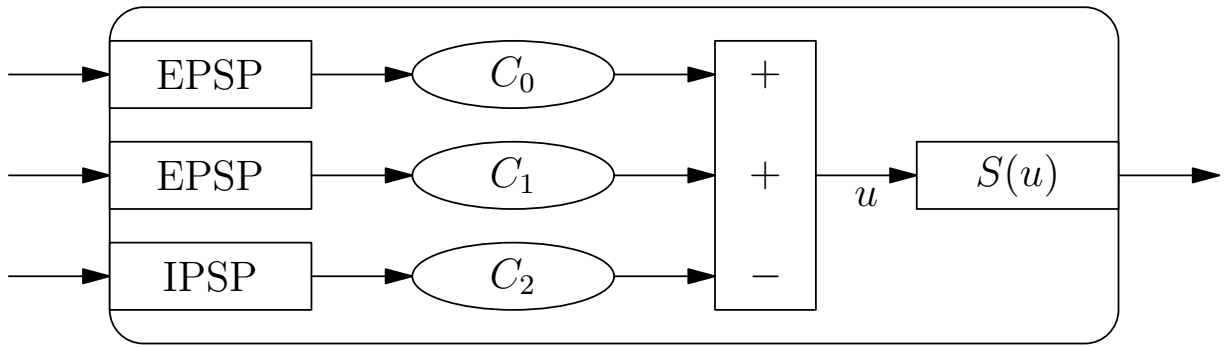
Figure 2.1: A schematic overview of a neural mass. Different inputs are converted to potentials using PSP transforms. These potentials are multiplied by a constant modeling the average number of synapses from this input to the population. Summing up all excitatory and subtracting all inhibitory potentials yields the average membrane potential u. Then a sigmoid transform is applied to u in order to get the average pulse rate that this population puts out.

This PSP transformation is used in nearly all later NMMs, for example [10, 17, 28]. In figure 2.2 an example of the impulse response h is plotted. It can be seen that the PSP transform has a peak. The time of this peak can be adjusted by the parameter q, since it lays at $t = 1/q$. The other parameter Q is used to tune the height of this peak that is given by Q/e.

The integral of the impulse function h in equation (2.1) is Q/q and depends on both Q and q. From a mathematical point of view one may prefer to tune this with a single variable $\widehat{Q} = Q/q$. In that case the impulse response becomes.

$$h(t) = \begin{cases} \widehat{Q}te^{-qt} & t \geq 0 \\ 0 & t < 0 \end{cases},$$

However in this case the maximum height of the peak in the impulse response is $\widehat{Q}/(qe)$ and this depends on two variables. This could be a reason that van Rotterdam et al. [27] used the impulse response of equation (2.1). Equation (2.1) has become the standard from then on. Also we will use the impulse response described by equation (2.1).

The impulse response in equation (2.1) corresponds to a linear transformation that is given by the following system of two ODE's:

$$\frac{\mathrm{d}x}{\mathrm{d}t} = y, \tag{2.2a}$$

$$\frac{\mathrm{d}y}{\mathrm{d}t} = Qqz - 2qy - q^2x. \tag{2.2b}$$

Here $z(t)$ is the input to the PSP transform and $x(t)$ the output of the PSP transform.

The potential-to-rate function converts the average membrane potential of a population, u, into an average pulse density. This average pulse density is the output of the neural mass. The potential-to-rate function is a non-linear function. It's usually taken to be a non-decreasing function that converges to zero as $u \to -\infty$ and is bounded from above. A common choice is a sigmoid function:

$$S(u) = \frac{2e_0}{1 + e^{r(v_0 - u)}}, \tag{2.3}$$

but also other functions are used for example in [18]. In equation (2.3) parameter e_0 is half of the maximal firing rate of the population, v_0 the average membrane potential for which half of the population fires and r a parameter for the steepness of the sigmoid. Most times $e_0 = 2.5$Hz, $v_0 = 6$mV and $r = 0.56$mV^{-1} are used. A graph of $S(u)$ for these values is plotted in figure 2.3.

With the description of the PSP transform and the potential-to-rate function we have discussed the basic principles that describe the behaviour of a single neural mass. In neural mass
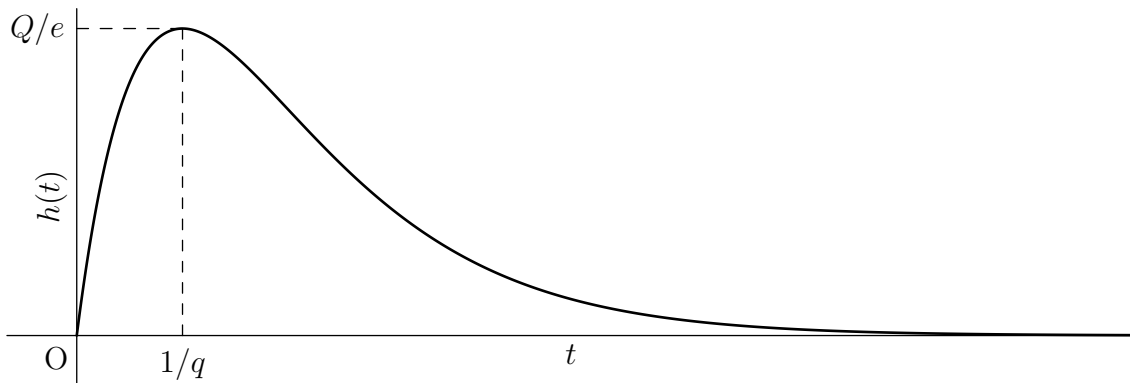
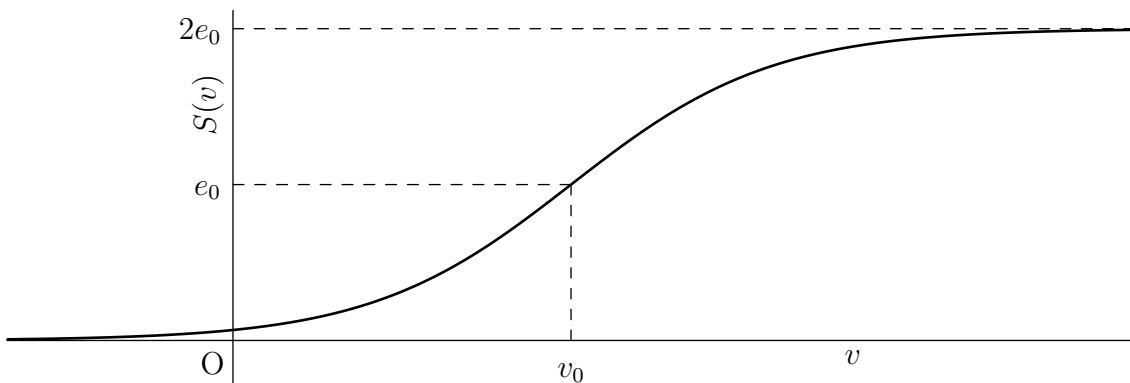Figure 2.2: Plot of impulse response function h.

Figure 2.3: Plot of the sigmoid function. It can be seen that for $v = v_0$ the sigmoid function has a value of e_0 and $2e_0$ is an asymptote.

models multiple neural masses are coupled to model bigger structures. In the next section we discuss the neural mass model by Lopes da Silva et al. [20] that models the thalamus. Later we will discuss different models for cortical columns.

2.2   Lopes da Silva's thalamus model

In 1974 Lopes da Silva et al. [20] published an article where models for the α-rhythm in the thalamus are investigated. In this article a neural network model is reduced to a NMM. First they consider a neural network model that consists of two classes of neurons namely thalamo-cortical relay cells (TCR) and interneurons (IN). Their neural network consists of 144 TCR neurons and 36 IN. With computer simulations is showed that this model is able to produce an α-rhythm.

In order to understand the influence of parameters they reduce this model to a neural mass model. Their neural mass model consists of two neural masses, one models the TCR, the other the IN. The TCR receive external excitatory input and inhibitory input from IN. The IN receive only excitatory input from the TCR. In figure 2.4 a schematic overview of this model is given.

The model by Lopes da Silva et al. [20] was adapted in further articles. As mentioned in the previous section Van Rotterdam et al. [27] proposed the impulse response of PSP transformation in equation (2.1). Let us indicate the parameters for the excitatory PSP with $Q = A$ and $q = a$ and for the inhibitory PSP one $Q = B$ and $q = b$. Van Rotterdam et al. [27] used $A = 3.25$mV, $a = 100$Hz, $B = 22$mV and $b = 50$Hz. These values have become the standard in most articles.
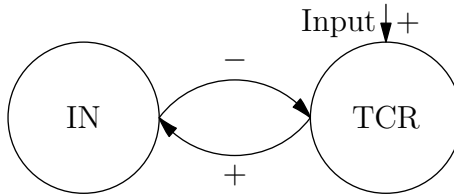
Figure 2.4: Schematic overview of Lopes da Silva's NMM for the thalamus. Arrows marked with + are excitatory connections, with − are inhibitory.

2.3 Models for cortical columns

In this section different neural mass models for cortical columns are discussed. Like the neural mass model by Lopes da Silva et al. [20] for the thalamus these models couple multiple neural masses together. The models for cortical columns that we discuss are based on the model by Jansen & Rit [17]. Therefore we will start with a description of this model.

2.3.1 Jansen & Rit model

In 1993 Jansen et al. [18] devolped a model for a cortical column that consist of three neural masses: pyramidal neurons, local excitatory and local inhibitory neurons. It was based on the model for the thalamus by Lopes da Silva et al. [20] and uses the PSP transformation as proposed by van Rotterdam et al. [27].

Two year later, in 1995, Jansen and Rit [17] used a slightly different version of this model that is the basis for most cortical NMMs. A schematic representation of this model is showed in figure 2.5. In the Jansen & Rit model pyramidal and local excitatory neurons give excitatory input to other populations where local inhibitory neurons give inhibitory input. Local excitatory and inhibitory neurons both receive input from the pyramidal cells with connectivity strength C_1 respectively C_3. Pyramidal neurons receive input from both excitatory and inhibitory neurons with connectivity constants C_2 respectively C_4.

In the Jansen & Rit model pyramidal cells are the only population that receive external excitatory input. This in contrast to the model by Jansen et al. [18]. Here also the local excitatory cells receive input from outside.

The external input to a cortical column can consist of output from pyramidal cells of other cortical columns and background activity. The model output that is studied is potential of pyramidal cells, since this is supposed to approximate EEG signals, as pyramidal neurons have by far the biggest influence on EEG signals.
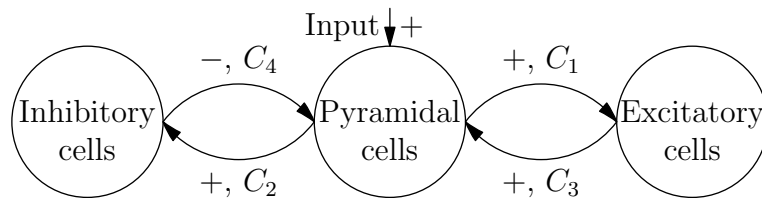
Figure 2.5: Schematic representation of the Jansen & Rit model for a cortical column. Arrows marked with + are excitatory connections, with − are inhibitory. The constants C_k, $k = 1, 2, 3, 4$ regulate the strength of the connections.

Jansen and Rit [17] related the connectivity constants in the cortical column by using literature on anatomical data of animals. In this way they found the following relation:

$$C_1 = C, \qquad C_2 = 0.8C, \qquad C_3 = C_4 = 0.25C, \tag{2.4}$$

with C a parameter. This parameter C is set to 135 in a large part of their work. Further the standard parameters for the sigmoid function are used: $e_0 = 2.5$Hz, $r = 0.56$mV^{-1} and $v_0 = 6$mV. As external input Jansen and Rit use noise that varies between 120 to 320Hz

Jansen and Rit [17] vary some parameters. They found out that their model was capable to produce activity types. These are displayed in figure 2.6. The upper left plot of this figure is what they called hyperactive noise. The potential of the pyramidal cells is high for this activity type. If the inhibition is increased the model produces a noisy α-rhythm and later on a normal α-rhythm. Then slow periodic activity with high amplitudes is seen. If the inhibition is higher the system produces hypo-active noise. The potential of the pyramidal cells is low in this case.

Wendling et al. [30] used the Jansen-Rit model with Gaussian white noise input with mean 90Hz. They claim to use a standard deviation of 30Hz, but probably this is much lower (see chapter 3.1). They observed that for $A = 3.25$mV the system oscillates in α-rhythm, when A is increased the model started to create sporadic spikes that become more frequent, till the system was only produce spikes.

Grimbert and Faugeras [12] investigated the influence of the stationary input I on the Jansen & Rit model using bifurcation analysis. They used the same parameter values as used by Jansen and Rit. In figure 2.7 the resulting bifurcation diagram is displayed. In this diagram the blue lines represent equilibria and the green lines the maxima and minima of periodic solutions. Solid lines indicate stable solutions and dashed lines unstable.

Grimbert and Faugeras found that the Jansen & Rit model has a large bistable region. For $0 < I < 89$ the system has 2 stable equilibria. At $I \approx 89$ one of these stable equilibria undergoes a Hopf bifurcation. This produces the stable limit cycle that is responsible for the α-rhythm. Between $I \approx 89$ and $I \approx 114$ the system has a stable equilibrium and the stable limit cycle producing the α-rhythm. At $I \approx 114$ a saddle-node on an invariant curve bifurcation (SNIC) takes place. This bifurcation produces a limit cycle with low frequency (< 5Hz) and the stable equilibrium disappears. The new created limit cycle generates Spike-Wave-Discharge (SWD) activity. Till $I \approx 137$ the α-rhythm limit cycle and the SWD limit cycle are the two stable solutions of the system. At $I \approx 137$ the SWD limit cycle disappears because at this point it undergoes a Limit Point of Cycle (LPC) bifurcation with an unstable limit cycle. From this point till $I \approx 315$ the α-rhythm is the only stable solution of the system. At $I \approx 315$ again a Hopf bifurcation takes place. The α-rhythm limit cycle disappears and for larger values of I the system has a stable equilibrium.

Grimbert and Faugeras [12] also consider briefly changes of other parameters. They concluded that varying parameters by more then 5% leads to drastic changes in the bifurcation diagram for I. Lower values of A, B and C or higher values of a and b make that the system no longer has stable limit cyles. Higher values of A, B and C or lower values of a and b give a new bifurcation diagram. The system is monostable for nearly all values of I and has a broader region (compared to the standard values) of SWD activity.

2.3.2 Variations on the Jansen & Rit model

In the literature there are a lot of variations on the Jansen & Rit model. In this section we consider some of these variations.

In 2002 Wendling et al. [28] proposed a modification of the Jansen & Rit model that is able to produce fast activity that is seen during seizure onset activity in epileptogenic brain regions. Based on bibliographic material they decided to split up the local inhibitory population in a fast and slow population. Therefore this model consists of pyramidal, local excitatory and fast and slow local inhibitory populations, see figure 3.1 on page 14. In this model all local population receive excitatory input from the pyramidal cells. The pyramidal cells in their turn receive excitatory input from the local excitatory cells and from outside. Further they receive inhibitory input from the fast and slow local inhibitory cells. In addition the slow inhibitory cells project inhibitory input to the fast inhibitory cells. The parameter q of the PSP transform for the fast
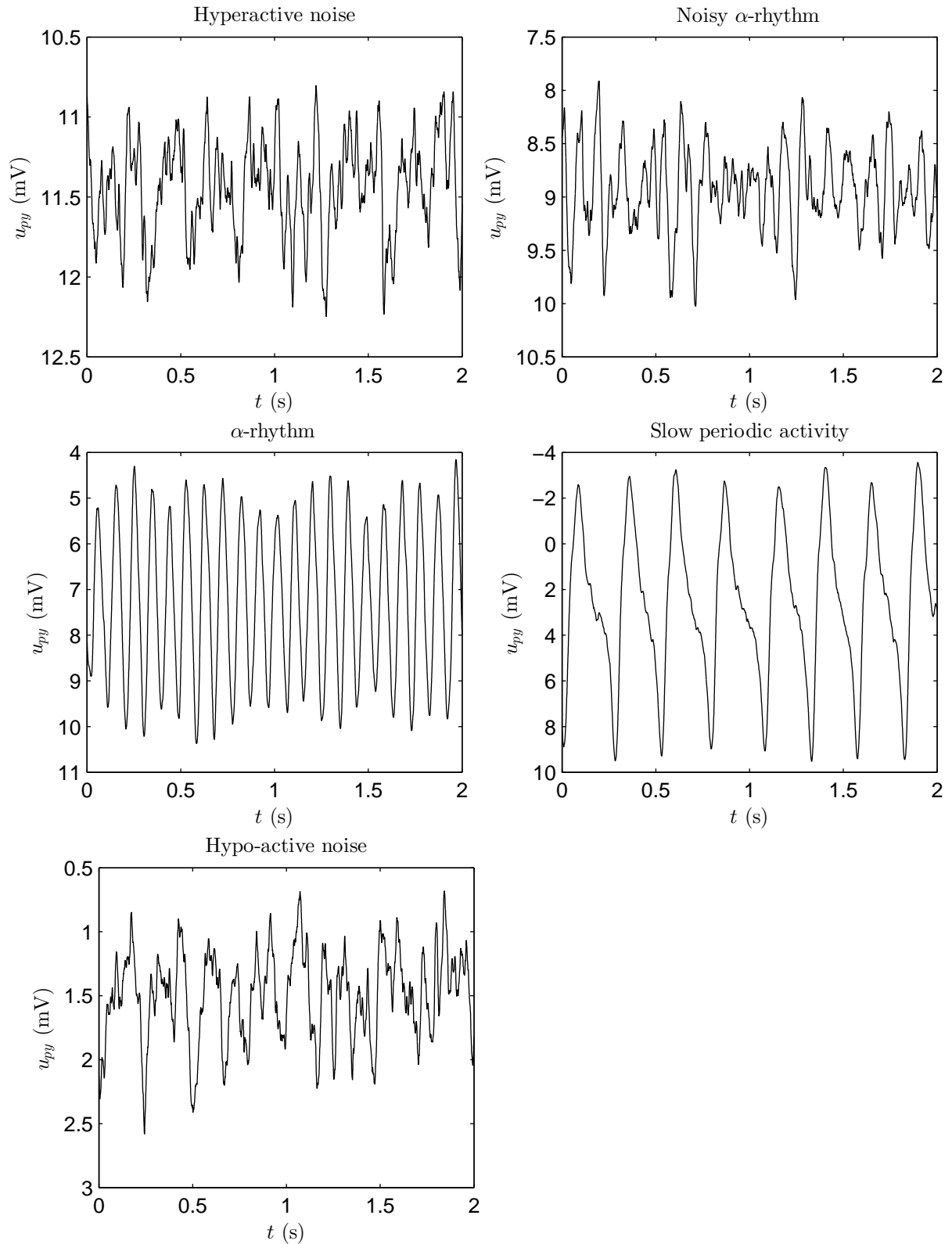
Figure 2.6: Time series for different activity types seen by Jansen and Rit [17] in their model. Top: hyperactive noise and noisy α-rhythm. Middle: α-rhythm and slow periodic activity. Bottom:hypo-active noise
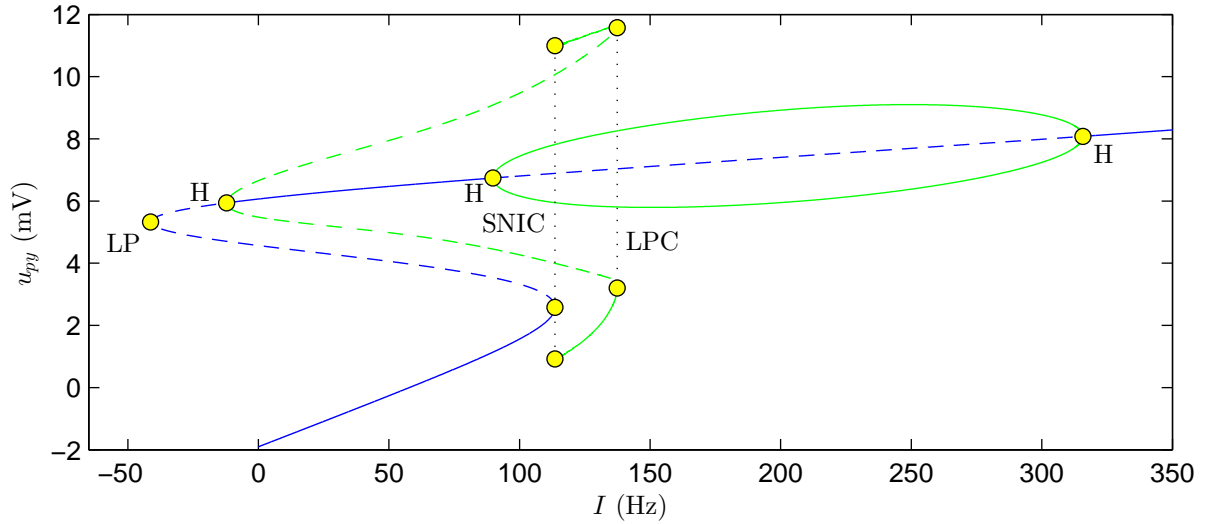
Figure 2.7: Bifurcation diagram of u_{py} as function of I for the Jansen & Rit's model as obtained by Grimbert and Faugeras [12].

inhibitory population is very high: $q = 500$Hz, so the time constant $1/q$ is very small. This is needed to produce the fast activity.

More information about the Wendling model can be found in chapter 3. Here we describe the result found by Wendling et al. [28] and other. Further we will give an overview of the different activity types that this model can produce.

A mix of the Jansen & Rit model and the Wendling model is considered by Goodfellow et al. [10]. A schematic overview of this model is given in figure 2.8. Goodfellow's model has, like the Jansen & Rit model, three populations. However they modeled a fast and slow inhibitory connection from the inhibitory cells to the pyramidal cells instead of only one inhibitory connection. Their target is to model the inhibitory process, that according to them has a highly variable time course, in a better way. The fast inhibitory PSP taken by Goodfellow et al. [10] uses $q = 200$Hz and is a lot smaller then in the Wendling model.

Goodfellow et al. [10] developed this model to generate SWD activity in a broad region. The model is also capable to produce oscillations with a frequency slightly lower then 15Hz. These oscillations are comparable with the α-rhythm in the Jansen & Rit model. Goodfellow et al. [10] call this background activity. Further this model is also able to generate poly SWD (multiple spikes followed by a slow wave) and other complex behaviour.
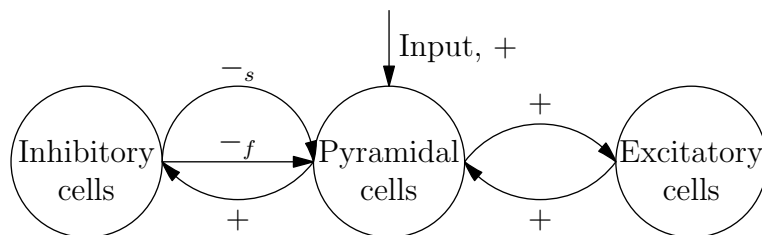
Figure 2.8: Schematic representation of Goodfellow's model [10] of a cortical column.

The model proposed by Goodfellow et al. [10] can be seen as a specific case of a class of models considered by David and Friston [5]. David and Friston generalized the Jansen & Rit model as displayed in figure 2.9. Each input to a population is split in n parts. All those parts a processed by their own PSP transformation that have their own parameters. In the figure we have $+_1, +_2, \dots, +_n$ for the excitatory PSP transforms and $-_1, -_2, \dots, -_n$ for the inhibitory PSP transforms. The factor ω_k is the fraction of synapses that is processed with PSP transformation

k. It holds that:

$$\forall_{k \in \{1, \dots, n\}} \omega_k \geq 0 \qquad \text{and} \qquad \sum_{k=1}^{n} \omega_k = 1.$$

So the constants C_1, C_2, C_3 and C_4 determine the total strength of the connections.
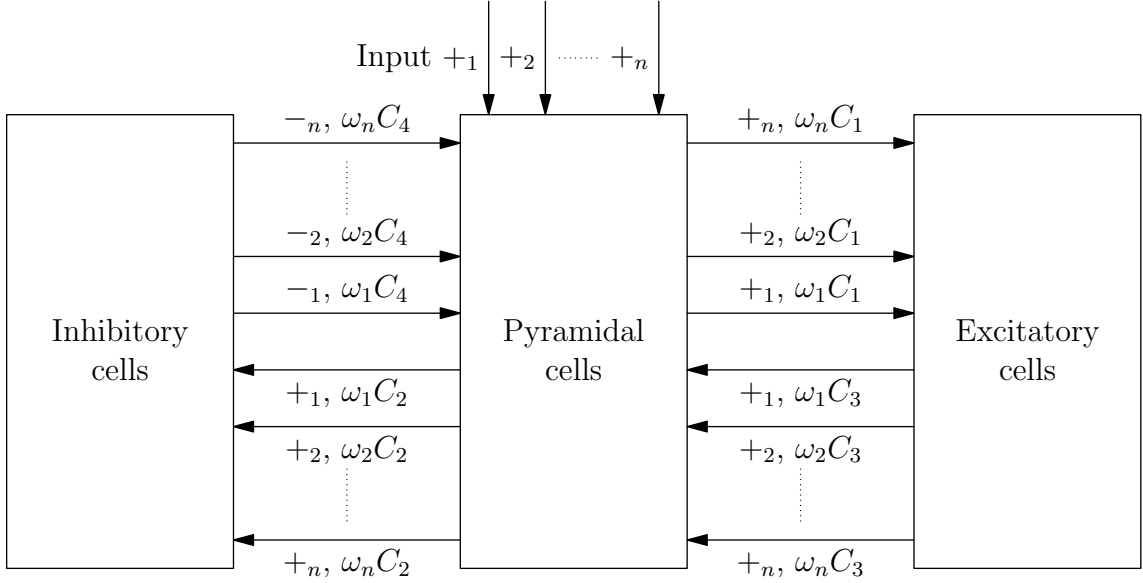
Figure 2.9: Schematic representation of David and Fristons generalization of the Jansen & Rit model.

David & Friston [5] investigate their model for $n = 2$. They took slow PSP transforms for $+_1$ and $-_1$ and fast PSP transforms for $+_2$ and $-_2$. The other parameters were chosen in such way that if $\omega_1 = 1$ or $\omega_2 = 1$ the systems oscillates in a frequency corresponding to the first resp. second PSP transform under stationary input. If they set $(\omega_1, \omega_2) = (\omega, 1 - \omega)$ and took $0 < \omega < 1$ the system was not oscillating with stationary input. However if a white noise input was applied then the started noisy oscillations. The frequency spectrum in those cases didn't have two separated peaks at the frequencies seen in case $\omega = 0$ or $\omega = 1$ but it had a single peak at some intermediate value, depending on ω.

In this section we discussed several models for a cortical columns. In the next chapter we will investigate one of them, the Wendling model, in more detail.

Chapter 3

Wendlingmodel

In the previous chapter we reviewed different neural mass models for cortical columns. In this chapter we investigate one of them, the model by Wendling et al. [28], in more detail. First a set of differential equations is derived that governs this model. Then is described what types of activity this model can produce and what their characteristics are. The next step is to investigate the influence of inhibition on the activity types. The target is to find boundaries between the different activity types. First this is done by bifurcation analysis. It turns out that not all the activity types can be separated in this way. Therefore we present a method to find the other boundaries. This leads to a map were different regions of activity are identified. Finally bifurcation analysis in a very broad parameter region is done in order to see what other type of behavior this model can produce and from which bifurcations they emerge.

3.1   Model formulation

The model proposed by Wendling et al. [28] consist of 4 neural masses: pyramidal cells, excitatory interneurons, slow and fast inhibitory interneurons. In figure 3.1 a schematic overview is given. The pyramidal cells give excitatory input to all other populations. They receive excitatory input from the excitatory cells and from outside. Further they receive slow inhibitory input from the slow inhibitory cells and fast inhibitory input from the fast inhibitory cells. The slow inhibitory cells give also a slow inhibitory input to the fast inhibitory cells.

The signs $+$, $-_s$ and $-_f$ along the connectivity arrows in figure 3.1 indicate what parameters for the PSP transform are used. The $+$ stands for the excitatory PSP transform. The parameters
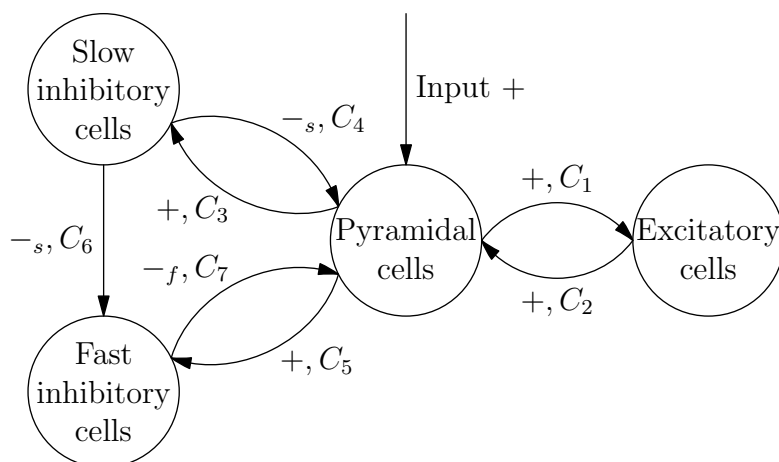

Figure 3.1: Schematic overview of Wendling's model for a cortical column.

Q and q in equation (2.2) for the excitatory PSP are taken to be $Q = A$ and $q = a$. The sign $-_s$ represent the slow inhibitory process. It's PSP transform has parameters $Q = B$ and $q = b$. Finally, the $-_f$ stands for the fast PSP transform, that has parameters $Q = G$ and $q = g$.

The parameters C_k, $k = 1, \ldots, 7$ are connectivity constants. It's useful to express these connectivity constants as fraction of a connectivity constant C. We have $C_k = \alpha_k C$, $k = 1, \ldots, 7$, where α_k, $k = 1, \ldots, 7$ are parameters that indicate the weight of the connection. The standard values for these parameters that are used by Wendling et al. [28] are found in table 3.1. These standard values are the same as those used by Jansen and Rit except for those that are not part of the Jansen & Rit model.

The Wendling model can be described by a set of eight differential equations using the differential equations in equation (2.2) that describe the PSP transformation. This leads to the following set of differential equations:

$$\dot{x}_0 = y_0, \tag{3.1a}$$

$$\dot{y}_0 = AaS(u_{py}) - 2ay_0 - a^2 x_0, \tag{3.1b}$$

$$\dot{x}_1 = y_1, \tag{3.1c}$$

$$\dot{y}_1 = Aa\left(\frac{I}{C_2} + S(u_{ex})\right) - 2ay_1 - a^2 x_1, \tag{3.1d}$$

$$\dot{x}_2 = y_2, \tag{3.1e}$$

$$\dot{y}_2 = BbS(u_{is}) - 2by_2 - b^2 x_2, \tag{3.1f}$$

$$\dot{x}_3 = y_3, \tag{3.1g}$$

$$\dot{y}_3 = GgS(u_{if}) - 2gy_3 - g^2 x_3, \tag{3.1h}$$

where

$$u_{py} = C_2 x_1 - C_4 x_2 - C_7 x_3, \quad u_{ex} = C_1 x_0, \quad u_{is} = C_3 x_0, \quad u_{if} = C_5 x_0 - C_6 x_2 \tag{3.2}$$

are the potentials of the pyramidal cells, excitatory cells, slow inhibitory cells and fast inhibitory cells. The parameter I stands for the external input to the cortical column.

The first two differential equations represent the excitatory input from the pyramidal cells to the other three populations. Because these three populations process the input from the pyramidal cells with the same PSP transformation this is possible.

The excitatory input to the pyramidal cells consist of excitatory input from the excitatory cells and input from outside the cortical column. These two inputs undergo the same PSP transformation. After the PSP transformation the potential contribution of the input from the excitatory cells needs to be multiplied by C_2 to account for the number of synapses. For the external input there is no multiplication constant needed, since such a constant can be absorbed in the input. After this those two are, together with the potential contribution from the two inhibitory inputs, added to form the potential of the pyramidal cells.

Because of the linearity of the PSP transformation we can change the order of addition and PSP transformation and the order of multiplication and PSP transform. This leads to the following process. First multiply the input from the excitatory cells with C_2. Then add the result to the external input and apply the PSP transformation. The advantage of this is that we need to apply the PSP transformation once instead of twice. Therefore we need two differential equations instead of four to describe the excitatory inputs to the pyramidal cells.

We change this a bit further. We want to apply the multiplication with C_2 of the excitatory input after the PSP transformation. However, if we do this, we also multiply the potential contribution of the external input with C_2. To solve this we divide the external input by C_2 before the addition. This gives I/C_2 term in equation (3.1d). The reason for multiplication after the PSP transformation is that the potential of the pyramidal cells, u_{py}, then is given by the

formula in equation (3.2). Here all the x's are multiplied with some C_k which gives a consistent formula.

The fifth and sixth equation model the slow inhibitory input from the slow inhibitory cells to the pyramidal cells and to the fast inhibitory cells. Finally the last two equations model the fast inhibitory input to the pyramidal cells coming from the fast inhibitory cells.

Note that in most articles where the Wendling model is used [2, 26, 28, 31] the model is described by a set of ten ODE's. In these systems of ODE's the slow inhibitory input to the pyramidal cells and to the fast inhibitory cells is modeled by two sets of two ODE's instead of one set of two ODE's.

As mentioned before, the parameter I represents the external input to the cortical column. Usually this input consist of a constant part and a stochastic part. In this chapter we set the constant part to 90Hz. The stochastic part is modeled as Gaussian white noise. This turns system (3.1) into a system of stochastic differential equations (SDE's).

To solve SDE's numerically one can't use methods for ordinary differential equations but adapted methods are needed. For example the Euler-Maruyama method or the Milstein method. Both are based on the plain forward Euler method. The Milstein method includes extra terms in comparison to the Euler-Maruyama method. It therefore has a higher order of strong convergence. However for the system of differential equations in (3.1) those two methods are the same, because the coefficient in front of the noise term doesn't depend on the state variables.

In the articles by Wendling et al. [28, 31] the standard deviation for the white noise is set to $\sigma_W = 30$. However, after trying to reproduce their results this seems way to big. In an other article by Wendling et al. [29] a link to the source code that can be used to simulate the Wendling model is given. It turns out that they used a plain forward Euler method to simulate the differential equations. Therefore the actually used standard deviation is:

$$\sigma = \sqrt{\Delta t_W}\sigma_W = \frac{1}{\sqrt{512}}30 \approx 1.33,$$

where Δt_W is the size of the time step that Wendling at al. [28, 31] used. The typical value was 1/512s (sampling frequency of 512Hz).

Here we will use $\sigma = 2$. This is slightly bigger then the standard deviation used by Wendling et al. [28] but still acceptable for the system. In the next section we will see what types of activity can be generated by the Wendling model.

3.2 Activity types

In their article Wendling et al. [28] distinguished six different types of activity in their system. These six types of activity where found by stochastic simulations of their model for parameters $(A, B, G) \in [0, 7] \times [0, 50] \times [0, 30]$. They separate these activities based on spectral properties and compared this with activity seen in depth-EEG signals.

In this section we first reproduce and describe these six activity types. After this it is showed that this model is capable to produce also other activity types. Part of these are found by Blenkinsop et al. [2]. We find two new types of activity. One of these is in the region explored by Wendling et al. [28].

For the simulation of the activity types we made an implementation for the system of differential equations in (3.1). This implementation uses the Euler-Maruyama method to numerically solve the differential equations and is written in Matlab. The source code can be found in appendix B at page 46.

Besides the time series also the frequency spectra of the different activities are plotted. Due to the noise term in the differential equations these frequency spectra are noisy. One can try to compute the frequency spectra in absence of noise, but some of the activities are noisy perturbations around a stable equilibrium state and don't show any activity in absence of noise.

Parameter	Description	Standard value
A	Average excitatory synaptic gain	3.25mV
B	Average slow inhibitory synaptic gain	22mV
G	Average fast inhibitory synaptic gain	10mV
a	Reciprocal of excitatory time constant	100Hz
b	Reciprocal of slow inhibitory time constant	50Hz
g	Reciprocal of fast inhibitory time constant	500Hz
C	General connectivity constant	135
α_1	Connectivity: pyramidal to excitatory cells	1
α_2	Connectivity: excitatory to pyramidal cells	0.8
α_3	Connectivity: pyramidal to slow inhibitory cells	0.25
α_4	Connectivity: slow inhibitory to pyramidal cells	0.25
α_5	Connectivity: pyramidal to fast inhibitory cells	0.3
α_6	Connectivity: slow to fast inhibitory cells	0.1
α_7	Connectivity: fast inhibitory to pyramidal cells	0.8
v_0	Sigmoid function: potential at half of max firing rate	6mV
e_0	Sigmoid function: half of max firing rate	2.5Hz
r	Sigmoid function: steepness parameter	0.56mV^{-1}

Table 3.1: Parameters and their default values as used in the Wendling model.

In order to get smoother frequency spectra we simulated $(n+1)10$s of model data. We neglected the first 10s of the output, in order to remove the effect of initial conditions. The other part is divided in n parts of 10s. For each part we computed the frequency spectrum after subtracting the mean. Then we averaged the results. The number of averaged parts, n, depends on the type of activity.

3.2.1 Activity types found by Wendling et al.

We now reproduce the activity types found by Wendling et al. [28] and try to give a clear description. We set $A = 5$ and varied B and G. The other parameters are set at their standard values as displayed in table 3.1. In figure 3.2 examples of the first four types of activity are given and in figure 3.3 the other two types of activity are given.

The activity that is called type 1 activity by Wendling et al. [28] is shown in the upper left plot of figure 3.2. This plot is made for $(B, G) = (50, 15)$ and for the frequency plot $n = 500$ is used. The activity can be described as a noisy perturbation around an equilibrium, because in absence of noise the system goes to an equilibrium. The frequency plot has a maximum around 5Hz. The power of this maximum is low because the activity is noise-driven. According to [28] this represents normal background activity.

Wendling et al. [28] don't mention that this activity type can be divided in two sub activity types depending on the mean value of u_{py}. We call type 1 activity type 1a if u_{py} is low (say < 2) and type 1b if u_{py} is high (say > 10). There is no type 1 activity seen for mid values of u_{py}. In case of type 1a activity the system is nearly inactive, all populations have a relatively low potential and therefore the pulse rate they send to each other is low. In case we have type 1b activity the system is almost saturated, most populations have a relatively high potential and therefore the pulse rate they send is high. There spectral properties of these subtypes are nearly equal.

Type 2 activity represents normal activity with sporadic spikes. It can be seen as type 1 activity with Spikes Wave Discharges (SWD) appearing now and then. The rate at which these SWDs appear depends on parameter values and also the standard deviation of the noise. The plot in figure 3.2 is made for $(B, G) = (40, 15)$. For the frequency plot $n = 1000$ is used. This

frequency plot shows a peak around 3Hz which is caused by the SWDs. Around 5Hz the decay of this peak show some irregularity. This is the effect of the period with normal activity.

The activity called type 3 consist of sustained SWDs. These SWDs are not very sensible for noise. This is because they are not generated by noisy perturbations around an equilibrium but by a limit cycle with large amplitude. This can also be seen in the frequency plot that shows a sharp peak with a high power around 4.5Hz. Other peaks are seen at multiples 2, 3 and 4 of this frequency. These higher harmonics arise because the limit cycle isn't a sinus-like oscillation. The frequency of the SWDs changes on parameter variation, the maximum frequency of the SWDs is roughly 5Hz. The example showed in figure 3.2 uses $(B, G) = (25, 15)$. For the frequency plot only 10 averages were needed.

Activity type 4 distinguished by Wendling et al. [28] is what they call slow rhythmic activity. As can be seen in figure 3.2, which uses $(B, G) = (10, 15)$, this activity shows some very noisy oscillations with highly varying amplitude. This is because the oscillations are noise-driven, in absence of noise the system goes to a stable equilibrium. The frequency of the oscillations changes a bit on parameter variation but lays around 10Hz as can be seen in the frequency plot that needed 200 averages.

An example of activity type 5 is given in the upper plot of figure 3.3. For this example we used $(B, G) = (5, 25)$ and $n = 500$. This activity is called low-voltage rapid activity by Wendling et al. [28]. As one can see in the plot, this type of activity features relatively irregular fluctuations with low amplitude, compared to the other activity types. The fact that the fluctuations have a low amplitude comes from the fact that this activity type is caused by stochastic fluctuations around an equilibrium state. This can also be seen in the frequency plot, because the maximum power that is observed is very low. A more interesting thing that can be seen in the frequency spectrum is that it has two local maxima. The first one appears at a very low frequency and is the result of noise. The second one is in the range 13-25Hz. Between those two maxima the power is relatively high, this makes that there is a broad frequency region with approximately the same power. In this activity type the influence of frequencies around 20Hz is relatively large, this is probably the reason why it's called rapid activity by Wendling et al. [28]. However, as we will see later, this model is also capable to produce activities with higher frequencies.

The last activity type distinguished by Wendling et al. [28] is activity type 6. In figure 3.3 an example of this activity type is displayed using $(B, G) = (15, 0)$ and only 10 averages for the frequency plot. Wendling et al. [28] call this slow quasi-sinusoidal activity. This activity consist of oscillations that have a high amplitude that is varying a bit. These small variations are effects of noise. In absence of noise this activity converges to a stable limit cycle and therefore produces oscillations that all have the same amplitude. The frequency of these oscillations is around 11Hz as the peak in the frequency plot indicates.

There are some relations between these activity types. Sometimes this makes it difficult to classify the right activity type. Type 4 and type 6 both show oscillations with a frequency around 10Hz. The criteria we will use is that type 4 activity is generated by random perturbations around an equilibrium state while type 6 is generated by a limit cycle. Further type 2 can be seen as a mixture of type 1 and type 3. It's difficult to formulate a clear boundary between those types. It depends on what you will call a 'sporadic spike' and is influenced by the standard deviation of the noise. In one of the next sections bifurcation analysis is done and based on this this we try to define the boundary between these types. However, first it is shown that also other types of activity can be found in the Wendling model.

3.2.2 Other activity types

Besides the six activity types found by Wendling et al. [28] there are also other types of activity present in this model. In [2] is showed that this model is capable to produce different types of poly SWD (pSWD) for high values of A and G that lay outside the region exploit by Wendling et al [28]. In figure 3.4 two different pSWD activities are shown. The first one has 2 spikes
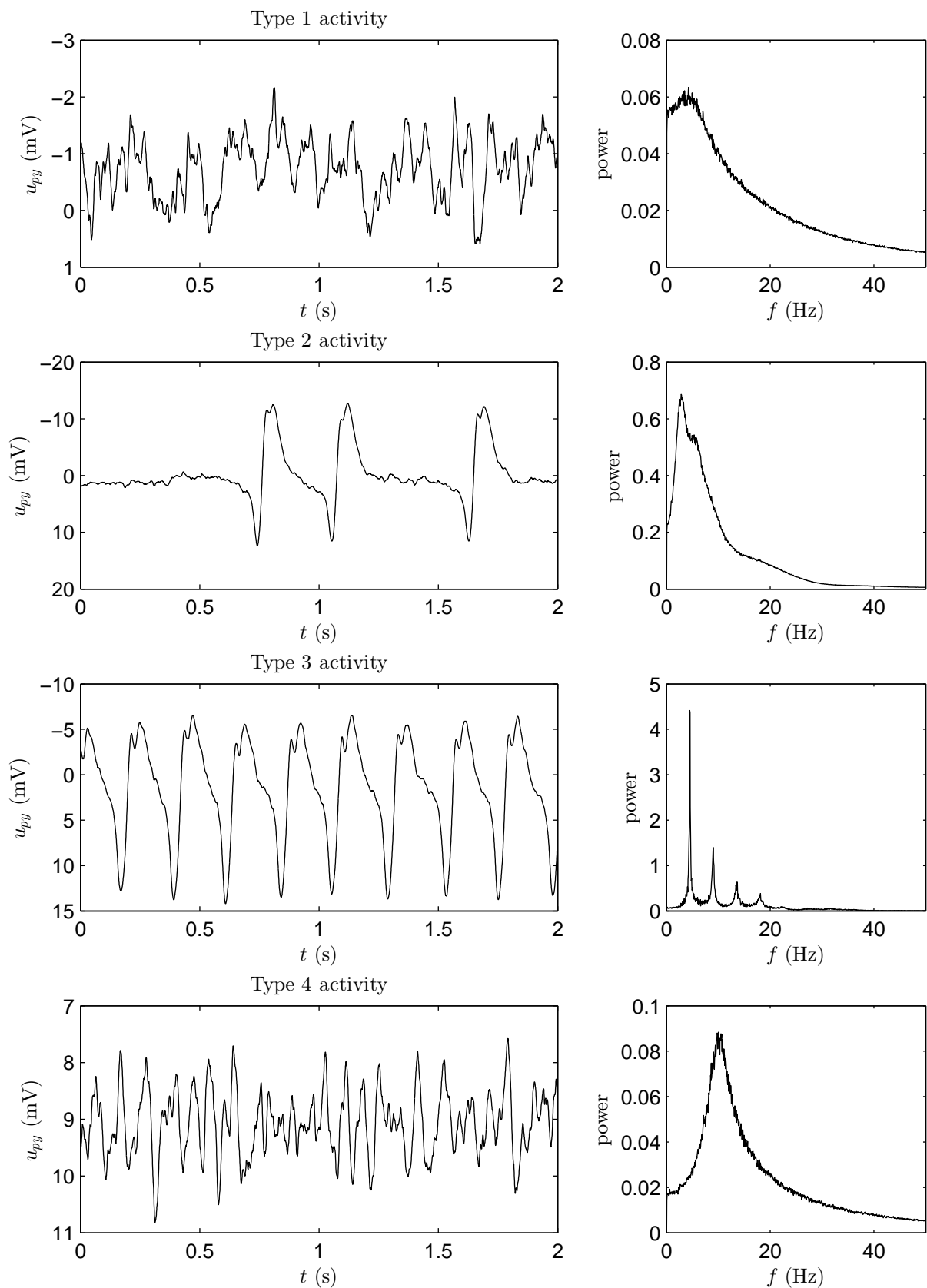
Figure 3.2: From above to bottom activity types 1 to 4. Left: typical time series. Right: frequency plot.
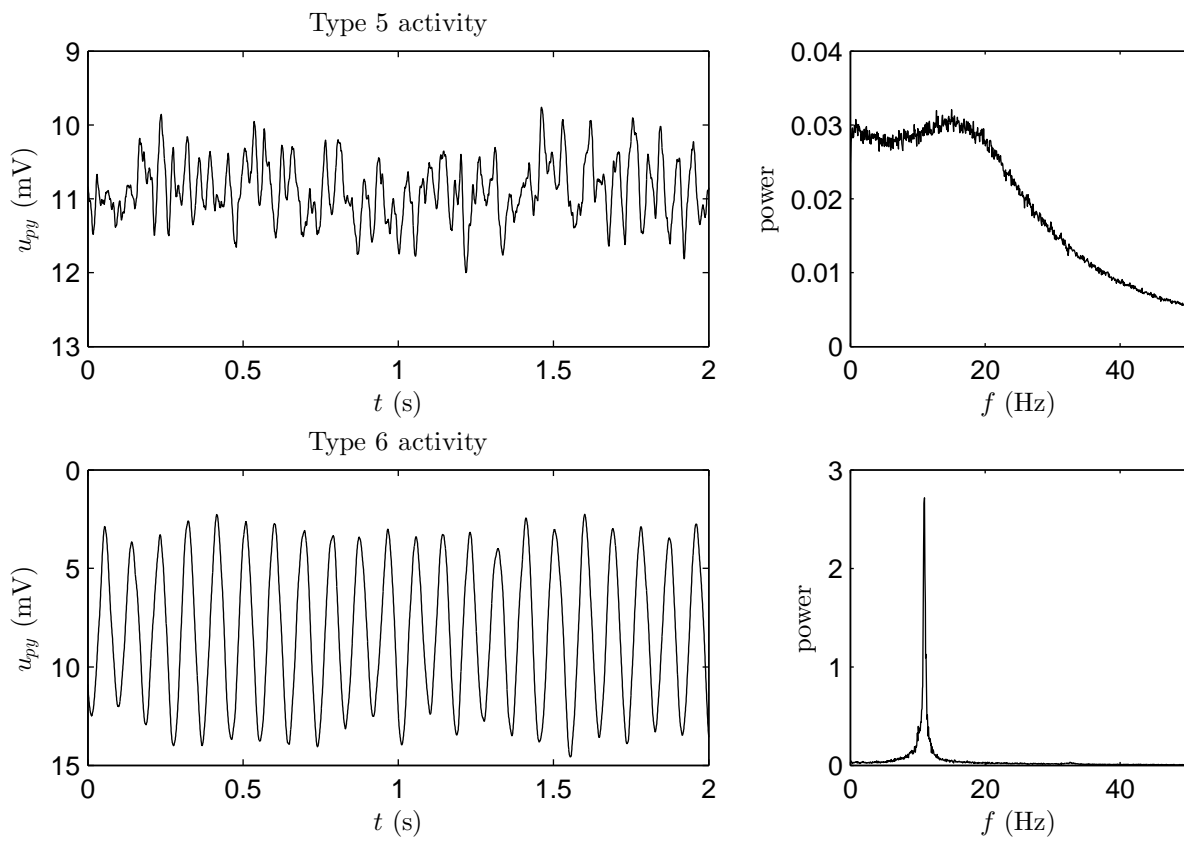
19

Figure 3.3: From above to bottom activity types 5 and 6. Left: typical time series. Right: frequency plot.
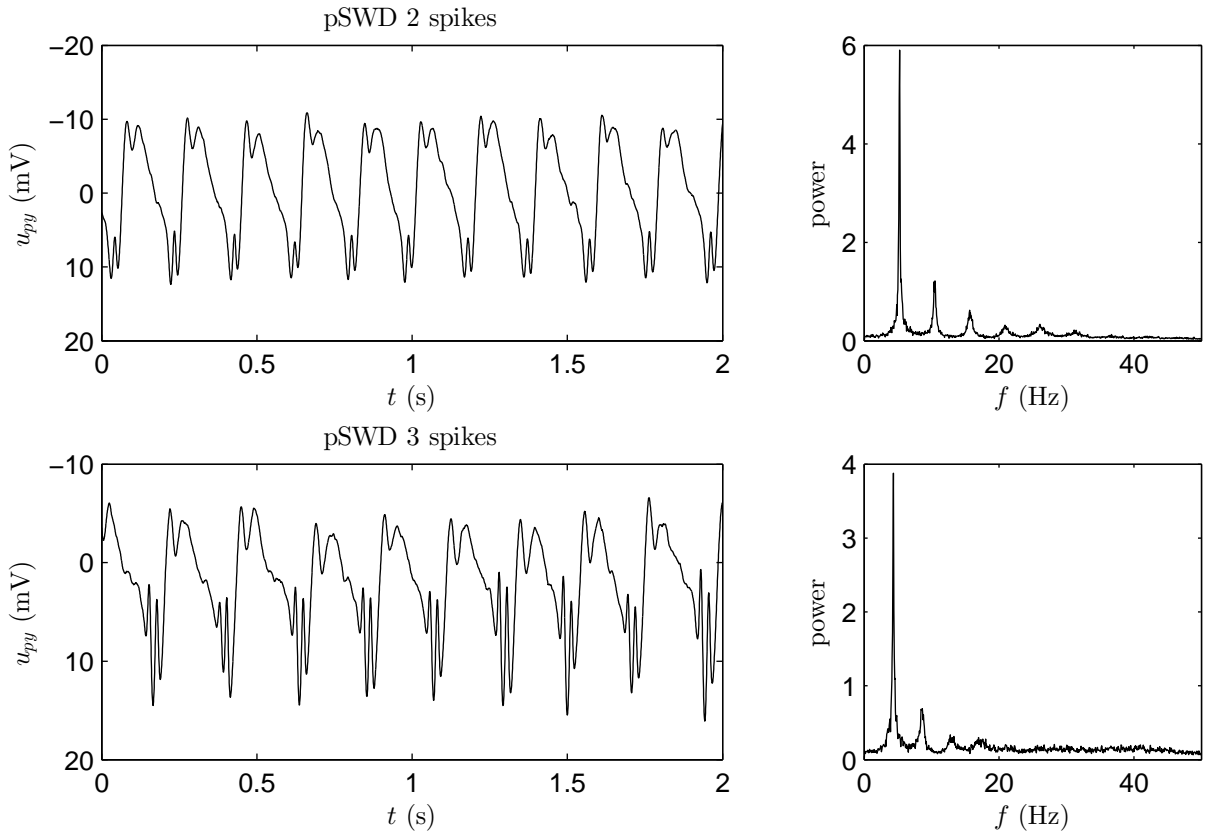
Figure 3.4: Two examples of pSWD activityies found by Blenkinsop et al. [2]. Top: 2 spikes, bottom: 3 spikes. Left: typical time series. Right: frequency plot.

followed by a wave. For this plot we used $A = 7$, $B = 30$ and $G = 50$. The other one has 3 spikes followed by a wave. For the example plot in figure 3.4 we used $A = 7$, $B = 25$ and $G = 150$. Both frequency plots are obtained with $n = 10$ and look like the frequency plot of the plain SWD case. Like the SWD activity also the pSWD activity is generated by a limit cycle. Besides the pSWD activity type Blenkinsop et al. [2] note that system is able to very complex types of activity in certain parameter ranges. According to them a lot of these activity types resemble wave forms that are seen in EEGs.

Neither considered in by Wendling et al. [28] nor by Blenkinsop et al. [2] are oscillations with a frequency of around 30-35Hz. These oscillations come in two different types of activity. The activity that we will call type 7 is displayed in the upper plot of figure 3.5. This activity can be compared to activity type 4. It are noisy oscillation that vary a lot in amplitude and have a frequency that is around 30Hz. The oscillations are noise-driven, because in absence of noise this system converges to an equilibrium. This activity type exists in a small part of the parameter region that is exploit by [28]. It uses a high value of G and a low value of B. For the plots in figure 3.5 $A = 5$, $B = 0$ and $G = 30$ is used. For the frequency plot 200 averages were needed.

The activity type that we will call type 8 is plotted in the lower plot of figure 3.5. For this example we used $A = 5$, $B = 0$, $G = 45$ and $n = 10$. In general this type of activity is visible for low values of B and values of G that are a bit bigger then those considered by Wendling et al. [28]. This activity can be compared with activity type 6 of Wendling et al. [28]. It is an oscillation with a relatively high amplitude that varies a small bit due to the noise. In absence of noise the system converges to a stable limit cycle with frequency 35Hz.
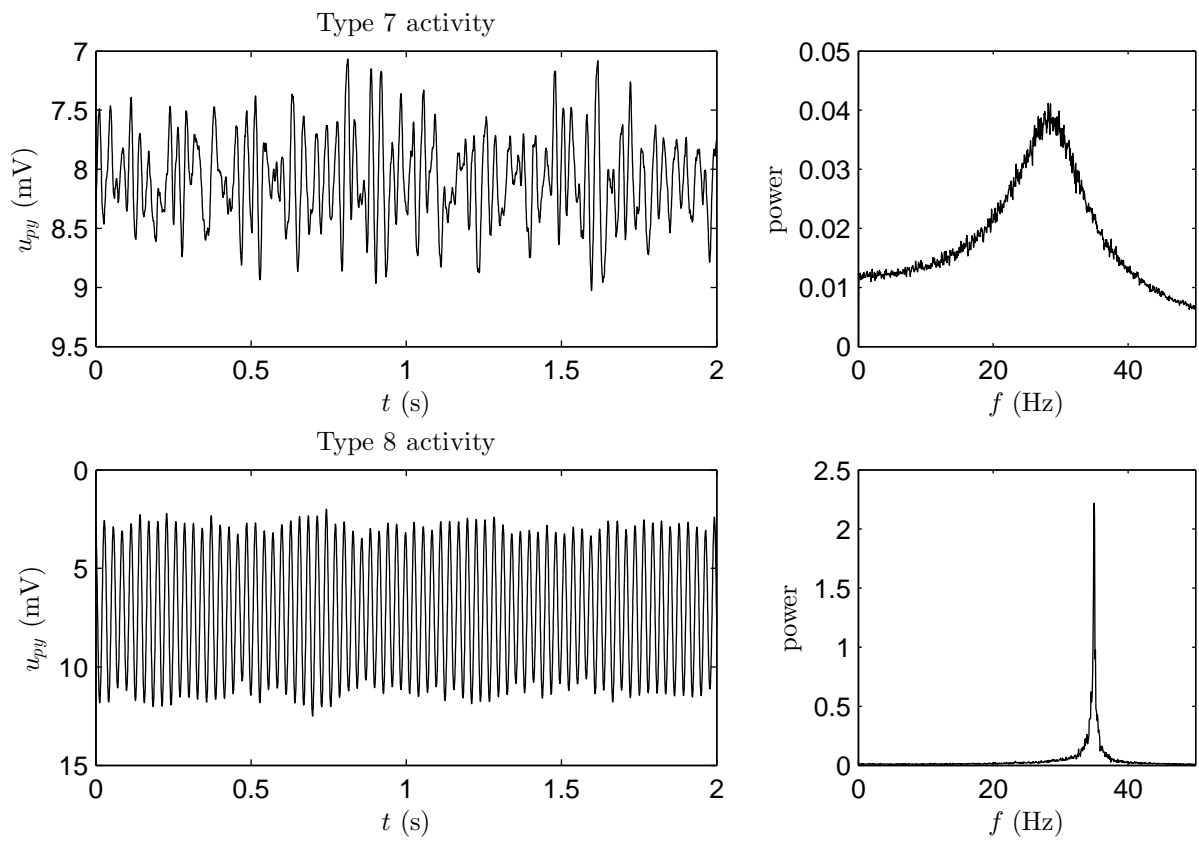
Figure 3.5: From above to bottom activity types 7 and 8. Left: typical time series. Right: frequency plot.
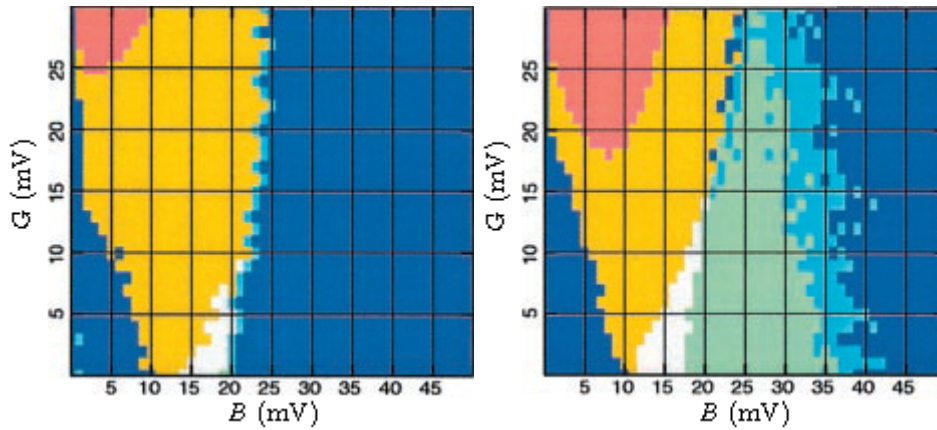
Figure 3.6: Activity maps, made by Wendling et al. [28], of the B-G-plane for $A = 3.5$ (left) and $A = 5$ (right). Type 1: blue, type 2: cyan, type 3: green, type 4: yellow, type 5: red and type 6: white. Images taken from [28].

3.2.3 Variation of synaptic gains

Based on their classification of activity types Wendling et al. [28] explored the activity types seen in the B-G-plane for various values of A by doing simulations for different parameter values. In this procedure parameter A was varied between 3 and 7 with stepsize 0.5. They varied B and G with a resolution of 1mV between 0 and 50 resp. 0 and 30. For every simulation they determined the activity type by looking at the frequency spectrum. In this way they obtained a colour map as displayed figure 3.6.

The colour maps in figure 3.6 are for the cases $A = 3.5$ and $A = 5$ those two are representative for the other maps. In both cases there are two regions of type 1 activity (blue). It turns out that the type 1 region at the lower left corner is type 1b and the region at the right is is type 1a.

The case $A = 3.5$ is representative for the activity maps for $A \leq 4$. In these maps there is no or a small region of type 2 activity (sporadic spikes, cyan) and type 3 activity (sustained SWD's, green). According to Wendling et al. [28] is the transition, that is seen if the border from the type 1b region (blue) to the type 4 region (yellow) is crossed, typically seen during ictal periods in brain regions that don't belong to the epileptic zone. A further property of the activity maps for low A is that it contains a small type 5 activity region. In case $A = 3$ this activity type isn't even visible.

The case $A = 5$ is representative for the activity maps seen for $A > 4$. It contains all the activity types that Wendling et al. [28] distinguished. The region with type 3 activity grows to the right (higher values of B) if A gets bigger. This causes also that the region of type 2 activity shifts to the right if A is increased, but the area of this region stays approximately equal. Further it can be seen that the type 5 region (rapid activity) grows.

Because Wendling et al. [28] did distinguish only six types of activity their maps don't contain activity type 7 that is visible in a small part of the region they explored. The example in figure 3.5 is also made for parameters that in this region. Type 7 is seen in the upper left corner of the red regions found by Wendling.

There are further differences between the activity maps of Wendling and the activity types we observe with our model. This is probably because the definition of the activity types we use here, is different from that used by Wendling et al. [28]. As far as it is clear from [28] they use only spectral properties. Our formulation of the activity types uses also the behavior under stationary input I.

In the next section we do bifurcation analysis on the Wendling model. We will use the results to find the boundaries between the activity types in the B-G-plane.
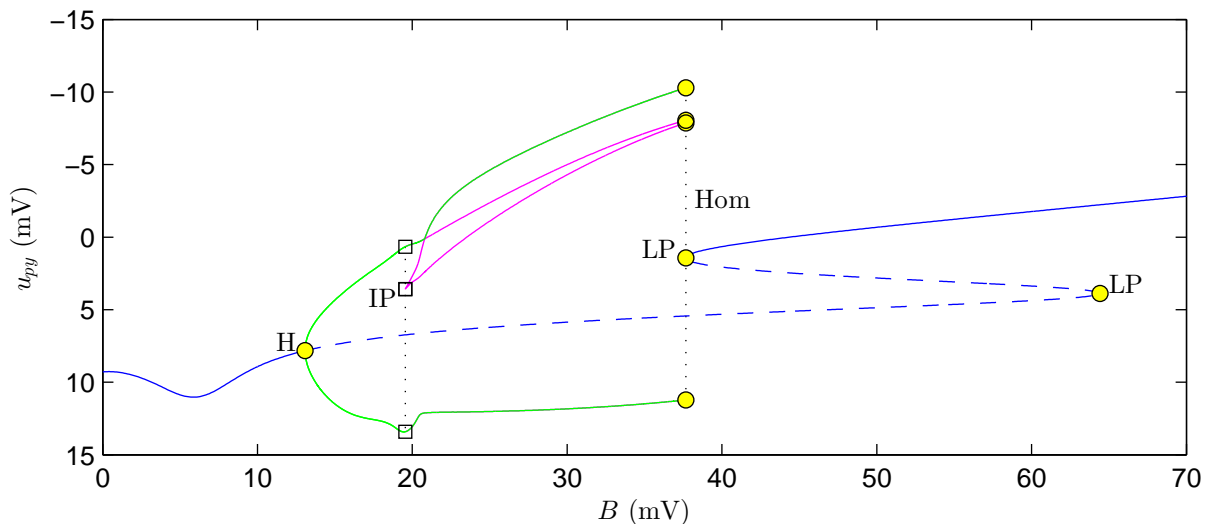
Figure 3.7: Bifurcation diagram of u_{PY} for continuation in B. Here we fixed $G = 25$ and $I = 90$. Blue lines indicate equilibria. Green lines indicate the minima and maxima of the limit cycle. The cyan lines indicate the local minima and maxima of the limit cycle that arises through the existence of spikes. Solid lines stand for stable solutions and dashed lines for unstable ones.

3.3   Bifurcation analysis in B

In this section bifurcation analysis on the Wendling model is performed. With the results we get more insight in the behaviour of the Wendling model under stationary input. It is also useful for finding the boundaries of the activity types for the model with white noise input. Bifurcation analysis on the Wendling model is done before by [2,26]. In [26] the focus is on continuation of I and C. Like [2] we will do continuation in B and G. We will find some new curves and give some new interpretations. Our focus will be at separating the different types of activity including the new types 7 and 8.

The bifurcation analysis is done using Matcont [8]. This is a package for numerical continuation in Matlab. During the bifurcation analysis A is fixed at $A = 5$ because for this value most types of activity can be seen. Further, it's assumed that the input I is constant with value $I = 90$, the mean value that is used if white noise is added.

In this section we will do bifurcation analysis in B while G is fixed at $G = 25$ or $G = 50$. This gives a part of the boundaries between the activities. It turns out that the others boundaries are no bifurcations. In the next section we present a new way to determine them.

3.3.1   Continuation in B for $G = 25$

Based on the activity map made by Wendling et al. [28] for $A = 5$ (see figure 3.6) we decided to do bifurcation analysis in B with G fixed at $G = 25$. This is done because this bifurcation curve will cross regions of different activity types.

In figure 3.7 we see what happens to u_{PY} if B is varied. Equilibria are indicated in blue. A solid line means that the equilibrium is stable and a dashed line means that the equilibrium is unstable. We see that for low values of B we have a stable equilibrium. At $B \approx 13.08$ a Hopf bifurcation takes place and the equilibrium gets two unstable eigenvalues. For $B \approx 64.42$ a limit point bifurcation takes place. At this point the curve turns 'backwards'. From there on the equilibrium has one unstable eigenvalue up to the second limit point that is found at $B \approx 37.66$. From here on the equilibrium point is stable again.

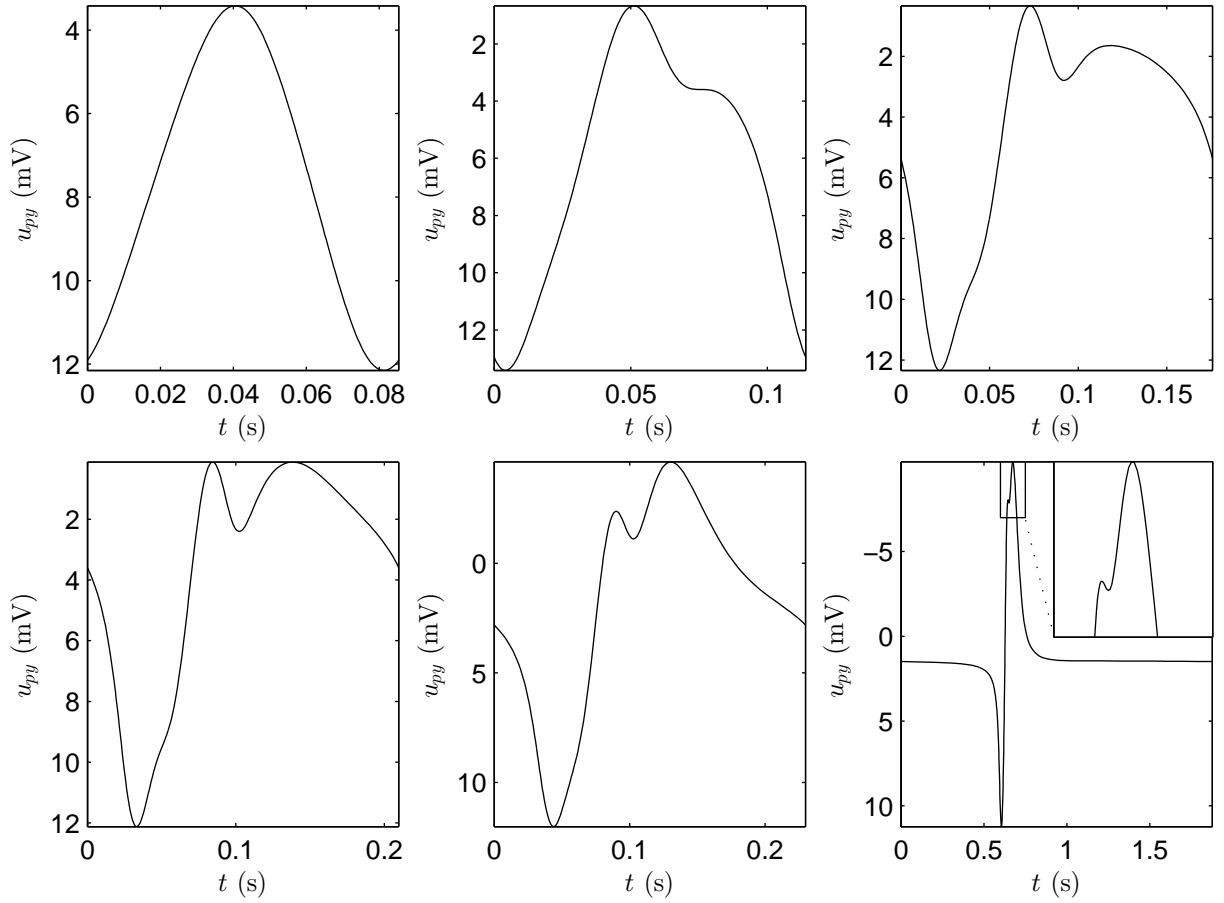From the Hopf point a limit cycle can be continued. Because the Lyapunov coefficient

Figure 3.8: Plot of limit cycles, u_{py} against time, for different values of B. Top row: $B = 16.0$, $B = 19.5$ and $B = 20.4$. Bottom row: $B = 20.8$, $B = 25.0$ and $B = 37.7$. Parameters A and G are fixed at $A = 5$ and $G = 25$.

of the Hopf point is negative a stable limit cycle will appear in the direction of the unstable equilibrium branch. In the bifurcation plot 3.7 the minima and maxima in u_{PY} of this limit cycle are indicated by the green curves. The magenta curves show local minima and maxima of the limit cycle.

Right after the Hopf bifurcation the time profile of the limit cycle has the shape of a sinus-like oscillation as can be seen in the upper left plot of figure 3.8. Therefore the limit cycle has a single minimum and maximum. The period of this oscillation is around 80 to 100ms which means that the frequency is between 10 to 12Hz. This can also be seen in figure 3.9, where the frequency of the limit cycle is plotted against B.

In the bifurcation plot (figure 3.7) it can be seen that at $B \approx 19.54$ a special point is marked with IP. At this point the limit cycle has an inflection point in u_{PY} as can be seen in the time profile of the limit cycle in the upper center plot of figure 3.8. This limit cycle has a point where the first and second derivative of u_{py} in time are zero, which means that the limit cycle has an inflection point. One can also observe in figure 3.9 that the frequency of the limit cycle goes down around the inflection point to approximately 5Hz.

An inflection point that appears in a limit cycle is not a bifurcation. At a bifurcation point the phase portrait of the dynamical system changes topologically [19]. This is not the case at an inflection point. A consequence of this is that the stability of the limit cycle isn't changed, the limit cycle remains stable after the bifurcation point.

However, what does change at the inflection point is our interpretation of the behavior of

the limit cycle. For values of B beyond the inflection point the limit cycle has two local minima and maxima instead of a single minimum and maximum. Hence, the geometry of the limit cycle has changed.

Due to this new minimum and maximum a spike is born. A spike is sharp positive deflection with a duration of 20-80ms [25]. In the upper right plot of figure 3.8 we see that there exist a sharp positive deflection between the global minimum and the local minimum (keep in mind that the y-axis is reversed as is usual for EEG signals). After this positive deflection u_{py} goes down till the local minimum is reached. After this the limit cycle continues his slow wave. In the bifurcation diagram 3.7 we indicated the maximum of the spike (local maximum) by a cyan line. Also the local minimum that exist due to the spike is indicated by a cyan line.

The non-global minimum decreases as B increases and at a given point it is as low as the global minimum. The limit cycle has two global minima as is displayed in the lower left plot of figure 3.8. After this point the non-global minimum switches to the other hole of the limit cycle. This gives the corner in the cyan line in the bifurcation diagram (figure 3.7).

If B goes up further the frequency of the limit cycle goes down to zero (see figure 3.9) or equivalently the period goes up to infinity. This is because the limit cycle approaches a homoclinic bifurcation. At this point the limit cycle becomes a homoclinic orbit and disappears for larger values of B. This homoclinic bifurcation takes place directly after the second limit point bifurcation of the equilibrium. For $G = 25$ these bifurcations don't fall exactly together so there is a region where both the limit cycle and an equilibrium point are stable. This region is very small, the difference in B value is less then 0.01. Therefore this region is not physiologically relevant. Later we shall see that there are larger values of G where the limit point and homoclinic bifurcation fall together and we have a so called Saddle-Node on an Invariant Curve (SNIC) bifurcation.

If we inspect the bifurcation diagram in figure 3.7 again we see that we now have described all bifurcations and curves. Therefore we will now give an interpretation of these results and compare them to the activity map of Wendling et al. [28] in figure 3.6. For low values of B the bifurcation diagram shows that the system has a stable equilibrium. This agrees with the fact that in Wendlings map activity type 4 and 5 are seen. Both these activity types arise from a stable equilibrium. The boundary between those two regions is not a bifurcation.

The Hopf point we found is the transition from a stable equilibrium to a stable limit cycle. In the definition we have given only type 3 (SWDs) and type 6 (α-rhythm oscillations) arise from a stable limit cycle. From the investigation of the limit cycle it turns out that right after the Hopf point type 6 is present and later on type 3 is seen. They are separated by the inflection point we found.

However if we compare this with Wendling's activity map (figure 3.6) we don't see activity type 6 for $G = 25$ but a direct transition from type 4 to type 3. This can be explained by the fact that type 4 and type 6 are closely related to each other. Type 4 consist of noise-driven oscillation with a frequency that is near to that of the limit cycle that causes type 6 activity. It's plausible that Wendling et al. [28] classified this as type 4 activity. Unfortunately, they don't give an explicit definition of their activity types, so we can't check this.

Further we found a homoclinic bifurcation of the limit cycle and a limit point bifurcation of the equilibrium that where close together. This can be seen as the transition between type 3 and an equilibrium activity type. Comparing with figure 3.6, which shows Wendling's activity map, it turns out that this must be the transition to type 1 activity. More precise it follows from the bifurcation diagram that the equilibrium value of u_{py} is low, so it is type 1a activity.

In Wendling's activity map the transition from type 3 to type 1 goes via type 2 activity. As indicated before, type 2 activity is a mix between type 1 and 3 and may come from a bistable region. However the bistable region we found in the bifurcation diagram is to small to explain the width of the type 2 activity region. A good reason for this can be the fact that for the bifurcation analysis the input $I = 90$ is constant while Wendling et al. [28] used Gaussian noise
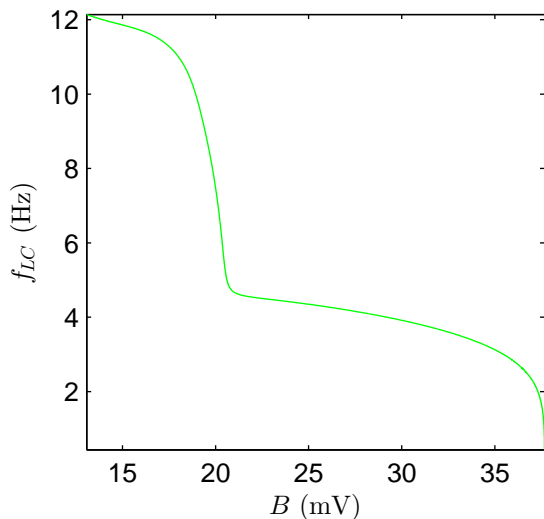
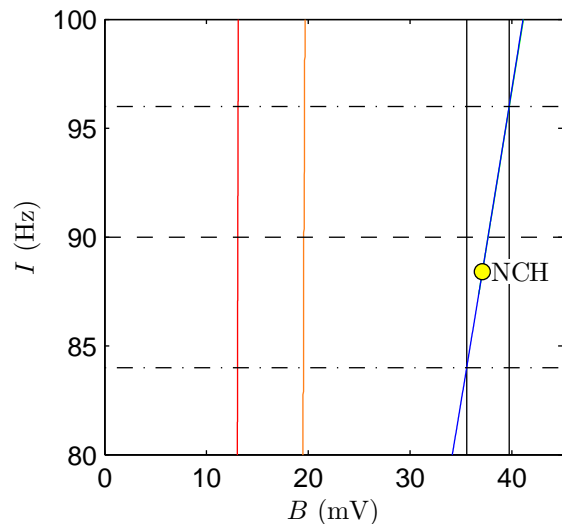Figure 3.9: Plot of frequency of the limit cycle as function of B.

Figure 3.10: Bifurcation diagram in B and I. Blue: limit point, red: Hopf, orange: inflection point. Horizontal lines indicate $I = 84$, $I = 90$ and $I = 96$. Vertical lines indicate the boundaries for which the blue line lays between $I = 84$ and $I = 96$.

input with mean $\mu = 90$. It therefore interesting to see what happens to the bifurcation points if I is varied, but still assumed to be constant.

In figure 3.10 the continuation of the Hopf point, inflection point and limit point in B and I is shown. One can see that the B value for which the Hopf bifurcation takes place almost stays constant if I varies. The same holds for the inflection point. This in contrast to the B value of the limit point. This is more sensitive to changes in I. The homoclinic bifurcation changes in the same way as the limit point bifurcation. Those two points stay close together. At $I \approx 87.2$ Matcont detects a Non-Central Homoclinic bifurcation, indicated with NCH in figure 3.10. At this point the homoclinic curve gets 'glued' to the limit point curve and they continue as a Saddle-Node on an Invariant Curve (SNIC) for lower values of I.

The curves in figure 3.10 divide the B-I-plane in a number of regions. In the region left of the Hopf curve (red line) the system has a stable equilibrium. Between the Hopf line and inflection point line (orange) the system has a stable limit cycle that looks like an α-rhythm oscillation. Between the inflection point line and the limit point line (blue) the system has the SWD limit cycle. Finally, right of the limit point line (and also right of the homoclinic curve that lies approximately on the limit point curve) the system has a stable equilibrium again.

It's known that about 99% of the Gaussian distribution lies between $\mu - 3\sigma$ and $\mu + 3\sigma$. In figure 3.10 these lines are indicated as horizontal black dash-dotted lines while the horizontal black dashed line indicates the mean value, $I = 90$. The two vertical black lines indicate the values $B \approx 35.65$ and $B \approx 39.74$. Between these values of B the limit point curve lays inside the zone $I = \mu \pm 3\sigma$. In this zone the system can jump from the SWD activity to equilibrium activity by varying I between $\mu \pm 3\sigma$. Hence in this region we can expect to see sporadic spike activity (type 2) if the system is perturbed with white noise.

One has to note that the bifurcation curves in figure 3.10 are valid for stationary values of I and don't tell exactly what happens if I varies as white noise. However it will give some indication where we can expect that due to the noise the system switches between SWD activity and fluctuation around a stable equilibrium. We therefore take the limit points for $I = \mu \pm 3\sigma$ as boundaries between type 1 and type 2 resp. type 2 and type 3 activity.

In this section we saw that for $G = 25$ we were able to find the boundaries between most of

the activity types. The only boundary that isn't found is the boundary between type 5 and type 4. This is because both activity arise from noise-driven perturbation around an equilibrium and the transition between those two is no bifurcation.

This holds for all boundaries between activity types that are noise-driven perturbations around an equilibrium (i.e. boundaries between type 1a, 4 and 5). If one wants to find boundaries between these types one need to find another method. This will be done in a later section.

First is looked at the bifurcation diagram for B with G fixed at $G = 50$, because it turns out that for this value of G the model has an interesting bifurcation diagram. The bifurcation diagrams for B with G fixed at a value lower then 25 are qualitatively the same as the bifurcation diagram in figure 3.7 and are therefore less interesting.

3.3.2   Continuation in B for $G = 50$

In this subsection bifurcation analysis in B is done while G is fixed at $G = 50$. In figure 3.11 the result of the bifurcation analysis is shown. The blue line in this figure indicate the value of u_{py} at an equilibrium point. A solid line indicates a stable solution and a dashed line an unstable one.

In contrast to the case $G = 25$ there is no stable equilibrium for low values of B. At $B \approx 4.13$ the equilibrium undergoes a Hopf bifurcation and becomes stable. The rest of the bifurcation diagram for the equilibrium point is qualitatively the same as in the case $G = 25$. The equilibrium has another Hopf bifurcation at $B \approx 14.19$ and becomes unstable. At $B \approx 64.31$ the equilibrium has a limit point. The equilibrium curve turns 'backward'. At $B \approx 34.81$ the equilibrium undergoes a SNIC bifurcation. The equilibrium becomes stable again and this remains the case for higher values of B.

From the Hopf point at $B \approx 4.13$ a stable limit cycle bifurcates in the direction of the unstable equilibrium. The minima and maxima of this limit cycle are shown by the green lines in figure 3.11. This limit cycle has the shape of a sinus-like oscillation and has a frequency of approximately 35Hz.

From the other Hopf point at $B \approx 14.19$ also a stable limit cycle bifurcates. Like in the case $G = 25$ this limit cycle shows first a sinus-like oscillation with a frequency in the α-band. A difference with the case $G = 25$ is that this limit cycle undergoes a period doubling bifurcation at $G \approx 21.53$. Here the limit cycle becomes unstable (see lower plot of figure 3.11). This unstable limit cycle has two inflection points, the first at $B \approx 22.4$ and the second at $B \approx 23.72$. After the second inflection point the limit cycle has 3 local minima and maxima. This limit cycle has a wave shape that can be seen as pSWD activity, it has two spikes followed by a wave.

The second inflection point is quickly followed by a period doubling at $B \approx 23.75$. After this point the limit cycle becomes stable for a short time, because at $B \approx 23.8$ the limit cycle has a limit point of cycle bifurcation. The curve of limit cycles turns 'backwards'. At $B \approx 23.52$ a second limit point of cycles is detected. The limit cycle becomes stable and the limit cycle curve turns 'forward' again. The stable limit cycle has another inflection point at $B \approx 27.29$. At this inflection point one local minimum and maximum disappears. After this inflection point the limit cycle has a SWD shape. This SWD limit cycle disappears at the SNIC point at $B \approx 34.81$.

From the period doubling points it's possible to continue a stable limit cycle with double period (not shown in figure 3.11). This limit cycle has a period doubling bifurcation quickly after it's birth and it becomes unstable. It's possible to continue an other limit cycle with double period (w.r.t the double period limit cycle) from this point. To continue this limit cycle numerically one need to increase the accuracy of the continuation. This is possible but the region in which this limit cycle exists is very small and not relevant to know for the activity types in the noisy system.

Now we have described all the different curves in the bifurcation diagram in figure 3.11 we try to interpret the meaning of the new bifurcations. The Hopf point for the low value of B
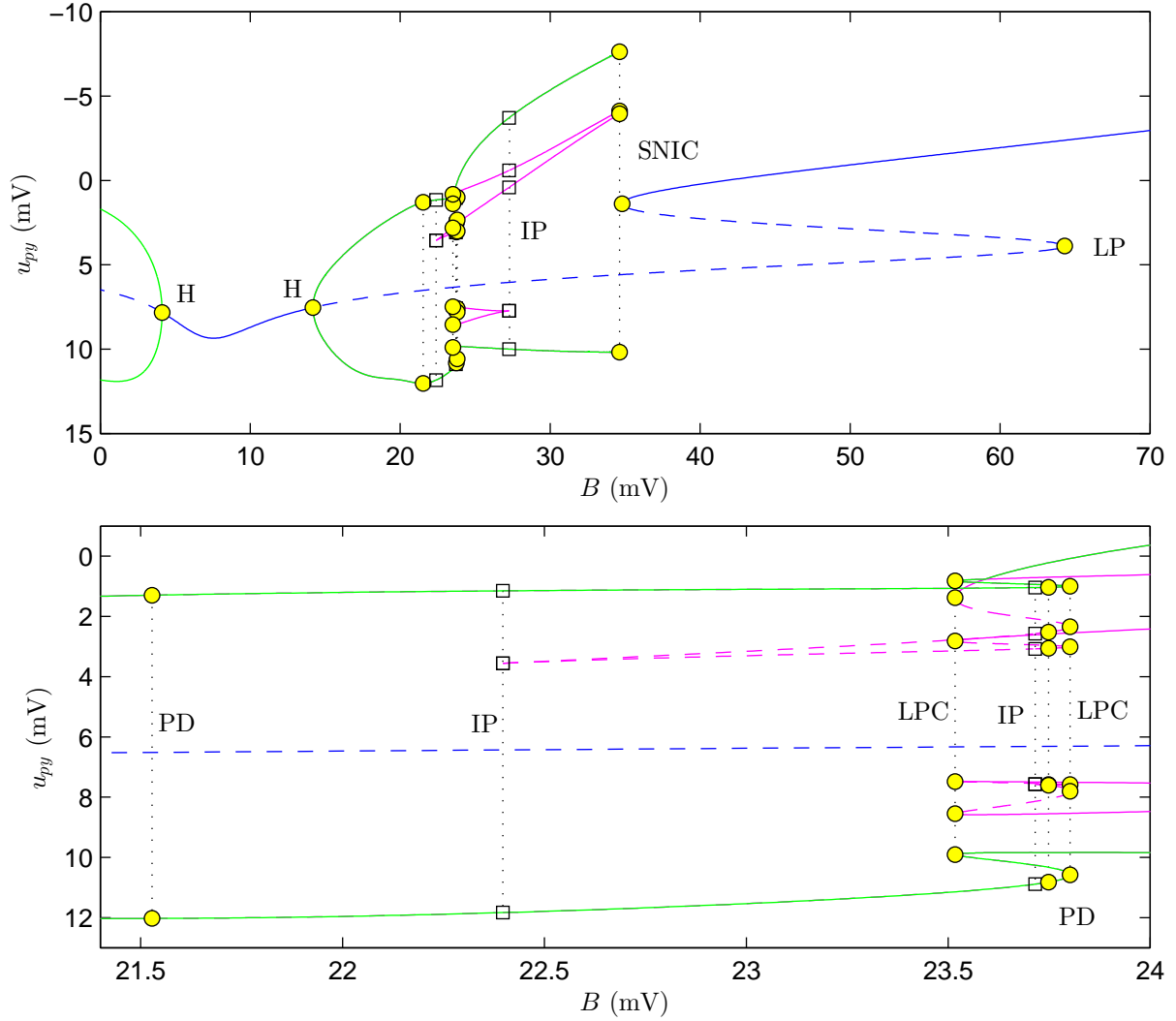
Figure 3.11: Upper plot shows a bifurcation diagram of u_{PY} for continuation in B while $G = 50$. Here we fixed $G = 50$ and $I = 90$. Blue lines indicate equilibria. Green lines indicate the minima and maxima of the limit cycle. The cyan lines indicate the local minima and maxima of the limit cycle that exist due to the spikes in the limit cycle. Solid lines stands for stable solutions and dashed lines for unstable ones. The lower plot is an enlargement of the upper plot to show the region around $B \approx 23$ in more detail.

can be seen as a boundary for type 8 activity. Since from this Hopf point a limit cycle with frequency in the γ-band bifurcates.

Further we found two period doubling points and two limit points. In the small region enclosed by these points the system has a chaotic behavior. Between the two limit points the system is bistable, while between the period doubling points there exist cycles with larger periods. One can expect that if noise is applied for parameters between the period doubling and limit points, the system shows complex wave forms.

Important is that the limit cycle has two inflection points in the period doubling and limit point region. Therefore the system generates pSWD activity with two spikes, as seen in the upper plot of figure 3.4, for values of B beyond the period doubling and limit point region. A third inflection point forms the boundary of this pSWD activity. After this point the system shows SWD activity.

In this section we have found a boundary for type 8 activity. However, as we observed also in the previous subsection not all bounds between activity types are bifurcations. We still want to find bounds for activity types that are generated by noisy perturbations about an equilibrium. This is done in the next section.

3.4   Boundaries between equilibrium activity types

In this section we will try to find criteria that can be used to separate activities that come from noise-driven perturbations around a stable equilibrium. As it turned out from the previous section these boundaries aren't given by bifurcations. There are no abrupt changes in stability that give a very sharp and clear bound. This also turns out from time simulations. If one makes time simulation for close parameter values one see a graduate change in activity rather than an abrupt change.

In order to find bounds for the equilibrium activity types we simulated some time series and frequency plots for $G = 13$, $G = 18$, $G = 23$ and $G = 28$ while we fixed $B = 3$. In the color map of Wendling 3.6 it can be seen that the line $B = 3$ passes through different regions of equilibrium activity types. The activity types for $G = 13$, $G = 23$ and $G = 28$ are relatively easy to classify with the description we gave before. They are classified as type 1a, type 5 and type 7 activity.

The case $G = 18$ is more difficult to classify. At first glance it's frequency plot doesn't show many similarities with that of the types we distinguished. The power of higher frequencies is not very high. Therefore this isn't type 5 or type 7 activity. For type 1b activity the power of the frequencies around 10Hz is too large. Then type 4 activity remains. The frequency plot doesn't have a clear peak around 10Hz. However, the frequencies around 10Hz do have a significant influence in the power spectrum. Therefore we will classify this as type 4 activity.

With these results in mind we try to find bounds for the equilibrium activity types. In the literature Blenkinsop et al. [2] suggested to look at the leading eigenvalue (eigenvalue with the smallest real part in absolute sense). The idea behind this is that the leading eigenvalues determines the behaviour of the dynamical system for the largest part. They state that activity type 5 comes from a leading eigenvalue that is real while type 4 activity comes from a complex leading eigenvalue. At the boundary between type 4 and 5 the system then has either a double real eigenvalue that is leading or a complex conjugated pair of eigenvalues and a real eigenvalue that are both leading. They don't mention a way to find the boundary between type 4 and type 1a.

In figure 3.13 we reproduced the curves where the system has a double real leading eigenvalue in the B-G-plane (green) and the curve where the system has both a leading real eigenvalue and a leading complex pair of eigenvalues (blue). This was done using continuation of an extend system of ODE's and is described in appendix A. The curves divide the plane in three different regions. The region we marked 'B1' is the region where, according to Blenkinsop et al. [2], type 1 and type 4 activity is seen. In region 'B2' activity type 5 could be seen. The activity in the
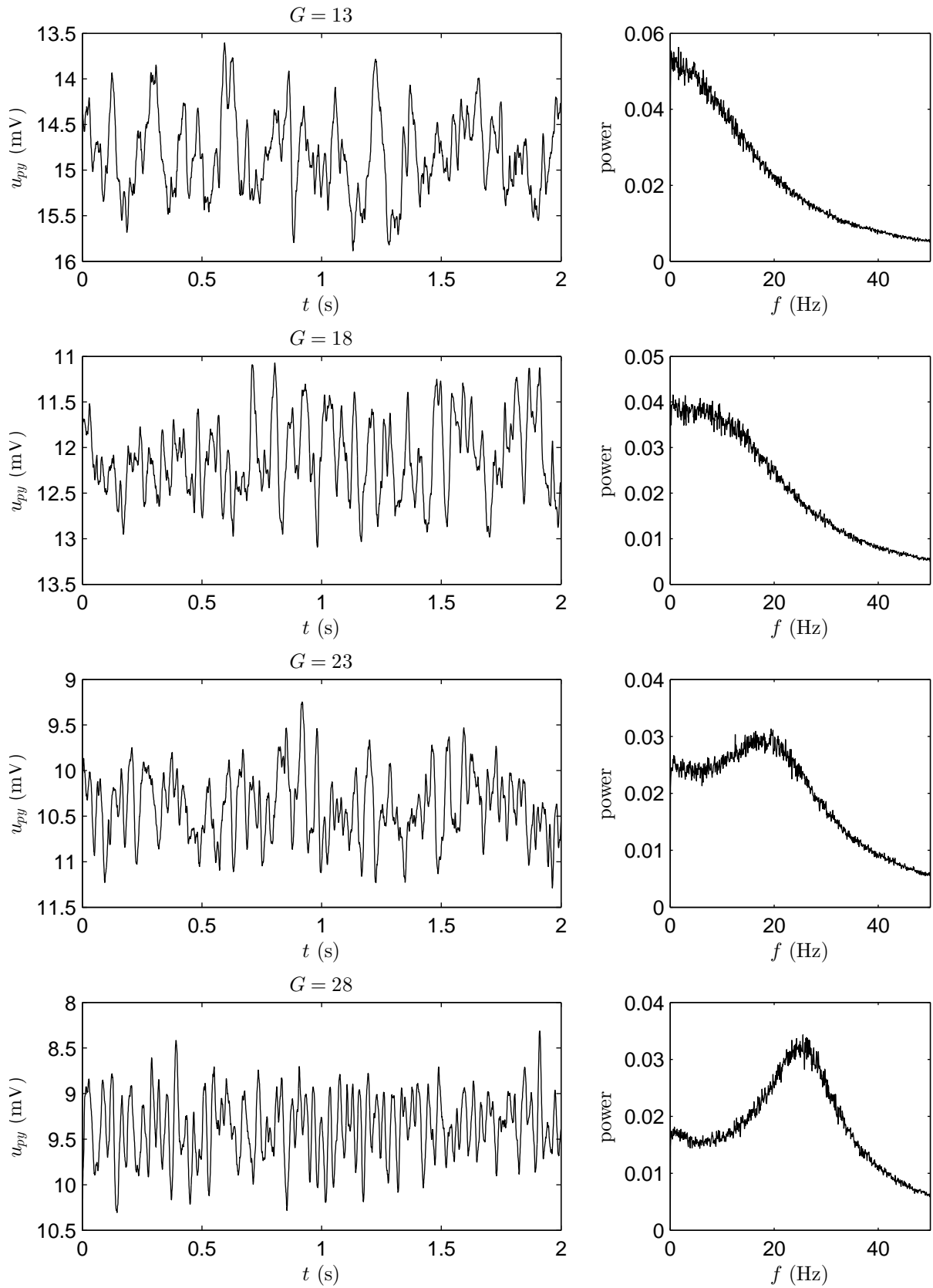
Figure 3.12: From top to bottom simulations for $G = 13$, $G = 18$, $G = 23$ and $G = 28$, while $B = 3$ for all plots. Left: typical time series. Right: frequency plot.
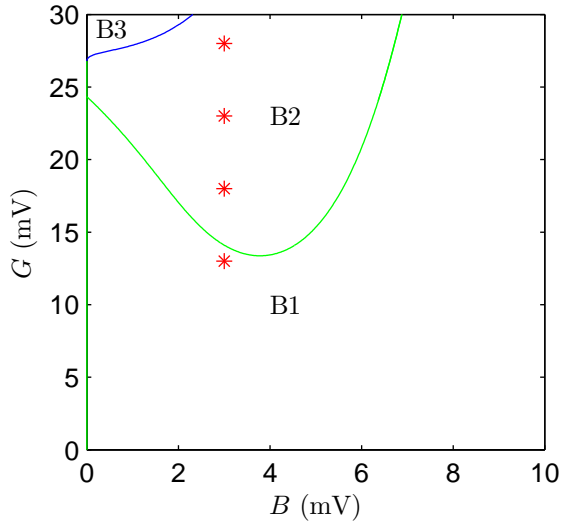
Figure 3.13: *B-G*-plot of boundaries proposed by Blenkinsop et al. [2] for activity type 5. Green line: double real leading eigenvalue. Blue line: leading real eigenvalue and leading complex eigenvalue pair. Red stars: parameter values used for plots in figure 3.12.
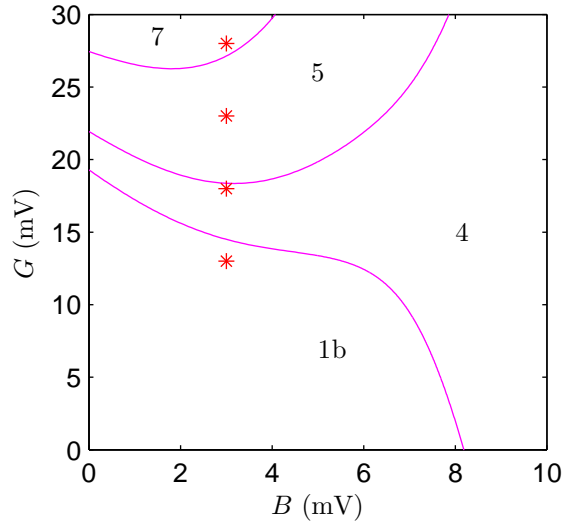
Figure 3.14: *B-G* plot of boundaries for the activity types proposed in this report. The curves show lines where the imaginary part of a certain complex eigenvalue pair is constant. Upper line correspond to imaginary part of $25 \cdot 2\pi$, middle line $13 \cdot 2\pi$ and lower line $7 \cdot 2\pi$.

last region 'B3' isn't mentioned but from our simulation we see that here type 7 activity is seen.

Let us now compare our classification of activity types we found for the plots in figure 3.12 with the region they are in according to Blenkinsop et al. [2]. In figure 3.13 the parameter values of the plots in figure 3.12 are indicated by red stars. It can be seen that the point $(B, G) = (3, 13)$ lays in region 'B1' as it should be. Also the plot for $(B, G) = (3, 23)$ (type 5) lays in the correct region, namely 'B2'. However the other points $(B, G) = (3, 18)$ (type 4) and $(B, G) = (3, 28)$ (type 7) should lay in regions 'B1' resp. 'B3' but this is not the case. One may attribute this to effects of the stochastic input but this differences are quite big.

We want to find better bounds then those proposed by Blenkinsop et al. [2] for activity type 5. Further we want also to find bounds for the other equilibrium activity types. In order to do this it may be a good idea to look at the eigenvalues of the equilibrium since the eigenvalues give information about the behavior close to the equilibrium.

Because our formulation of the Wendling model in equation (3.1) has 8th ODE's we have 8 eigenvalues. These eigenvalues can only be computed numerically. It turns out that 4 of the eigenvalues don't vary much if B and G are changed. Two of them form a complex conjugated pair of eigenvalues with a real part around -500. The other two are real eigenvalues and vary around -100.

The other four eigenvalues change a lot more if B and G are varied and have nearly every where a larger real part then the first four. Two of these eigenvalues are always a complex conjugated pair, the other two could be both real or a complex conjugated pair. In figure 3.15 the real and complex part of these four eigenvalues are shown if G is varied and $B = 3$.

It can be seen that for low values of G the four eigenvalues are all complex. The pair with the larges real part splits around $G \approx 14$ in two real eigenvalues. At this point the transition from a leading complex pair of eigenvalues to a leading real eigenvalue takes place. This can also be seen in figure 3.13 as the intersection between the line $B = 3$ and the green line. After this transition one eigenvalue increases and the other decreases.

The other two eigenvalues that are plotted in figure 3.15 form a complex conjugated pair of eigenvalues for all parameter values. The real part of this pair lays around -100 for values of G below 10. For larger values of G the real part increases a lot. Around $G \approx 21$ it becomes bigger
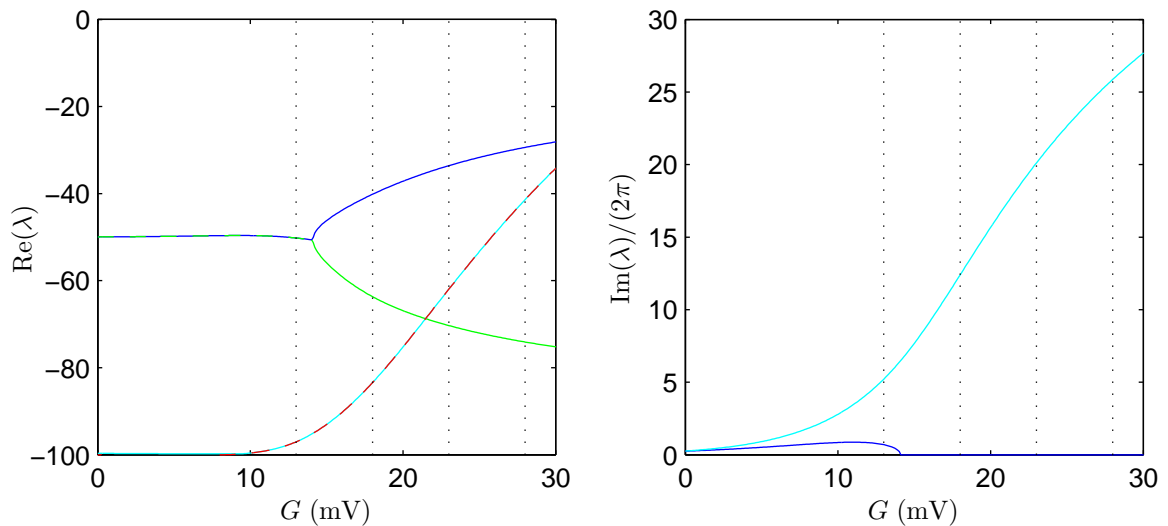
Figure 3.15: Plots of 4 eigenvalues with larges real part if G is varied and $B = 3$. Left: real part. Right: imaginary part divided by 2π.

then smallest real eigenvalue. For $G = 30$ the real part is close to the largest real eigenvalue. Not shown in the plot is that for larger values of G this pair of complex conjugated eigenvalues becomes the leading eigenvalue pair and if G is increased further this pair of eigenvalues becomes unstable and generates a Hopf bifurcation. This Hopf bifurcation is responsible for the birth of the limit cycle that generates type 8 activity.

In the right plot of figure 3.15 the complex part of the eigenvalues divided by 2π is plotted. The division by 2π is done because then complex part of the eigenvalues matches with the frequency that it can generate. One can see that the frequency, of the eigenvalues that form a complex pair all the time, increases from nearly 0 to nearly 30 if G increases. The frequency of the other complex pair stays low as long as it exists.

Let's try to see how the influence from the eigenvalues is visible in the time series and frequency plots in figure 3.12. The frequency plots for $G = 23$ and $G = 28$ have a peak in the power spectrum at a frequency that is very close to the imaginary part of the eigenvalue pair that is complex all the time divided by 2π. The difference can be explained by stochastic effects of the input that causes the frequency spectrum to be noisy.

For the other two cases displayed in figure 3.12 (for $G = 13$ and $G = 18$) this correspondence is less clear. The frequency plot of these cases doesn't have a clear peak in the frequency spectrum. This can be explained by the fact that the real part of the complex conjugated eigenvalue pair is small here compared to the real part of the leading eigenvalue. Therefor this eigenvalue has less influence on the system then in the cases $G = 23$ and $G = 28$. However it has a small influence. In case $G = 18$ the frequency spot has a relative large range of frequencies where the power is close to the maximum power. This can be a consequence of the eigenvalue with large complex part that would correspond to a frequency of around 12Hz in this case.

With a bit of fantasy the same argument hold for the case $G = 13$. There the frequency induced by this complex conjugated eigenvalue pair is around 5Hz. Another interesting thing in case $G = 13$ is that also the leading eigenvalue is complex as can be seen in figure 3.15. It's complex part is very small and corresponds to a frequency of 0.7Hz. This peak is close to 0 and is difficult to see in the plot.

From our observation we can conclude that the imaginary part of the complex conjugated eigenvalue pair that always exist has a significant influence on the frequency plots in figure 3.12. The value of the imaginary part divided by 2π gives an indication the main frequency observed in the system. Therefore it is a good idea to use this as criterion for the boundary between the

33

equilibrium activity types.

It's a good question what frequency forms the bound between two activity types. Activity type 7 that we distinguished can be seen as a noisy γ-rhythm. Therefore we decide to use the frequency bounds for the γ-rhythm as a bounds for activity type 7. Wendling et al. [28] use a frequency range between 20-100Hz for the γ-rhythm based on [3]. In an overview article by Hughes [16] 25Hz is used as lower bound for the γ-rhythm. In this article it's also mentioned that other lower bounds for the γ-rhythm are used, and that it was earlier defined as a rhythm around 40Hz. We decided to use 25Hz as lower bound for activity type 7, also because we observed in the frequency plots that the maximum power goes down a lot if the maximum power lays around 25Hz.

Activity type 4 can be seen as an α-rhythm oscillation. In [1] the α-rhythm is said to lay in the range 7-13Hz, [20] uses 8-13Hz and David and Friston [5] uses 8-12Hz based on [22]. These values all differ a bit but not much. Based on this we decide to use a frequency range of 7-13Hz for activity type 4.

This also fixes the ranges for activity type 1b and type 5. Activity type 1b has a lower frequency then type 4 so we take this as < 7Hz. Activity type 5 lays between type 4 and type 7 and is therefor in the range 13-25Hz.

We continued the boundary curves between the activity types in the B-G-plane using Matcont. We therefore used an extended system of ODE's that continues curves where the imaginary part of a complex conjugated eigenvalue pair is fixed. A precise description of this method can be found in appendix A. In figure 3.14 the boundaries we found between the activity types in the B-G-plane are displayed. In this figure also the parameter values of figure 3.12 are plotted with a red star. It can be seen that the activity type regions correspond to the activity type we classified the plot in figure 3.12.

3.5   Activity map for the B-G-plane

In section 3.3 we did bifurcation analysis in B for fixed values of G. In this way different codim 1 bifurcations were found: Hopf, limit point and homoclinic bifurcations. We saw that these bifurcations form the boundary between some of the activity types. Further we also found out that a limit cycle could have an inflection point that gives a false bifurcation. This false bifurcation is the boundary between type 6 and type 3 activity. In the previous section we discussed how we could find suitable borders between the other activity types, which all came from noisy perturbations around a stable equilibrium, and presented a way to continue them in two parameters. In this section we will put these results together.

Using Matcont we continue the codim 1 bifurcations, which we found with the bifurcation analysis in B, in B and G. We also want to continue inflection points in two parameters. Since an inflection point is not a bifurcation, there is no direct method implemented in Matcont to do this. In [23] a method for continuation of inflection points of limit cycles is proposed using a periodic boundary value problem. They provide a link to an implementation for DDE-BIFTOOl (another package for numerical bifurcation analysis), but unfortunately this isn't available anymore.

To find a reasonable approximation of the inflection point curve in B and G we use the following method. We continue from a large number of points at the Hopf bifurcation curve, a limit cycle in B. For each of these limit cycle curves we detect the value at which the limit cycle gets an extra maximum. In this way we obtain values of B and G that approximate the inflection point curve.

The continuation of the codim 1 bifurcations, the inflection points and the boundaries for the equilibrium activity types are displayed in figure 3.16. Here a map for the different activity types for $(B, G) \in [0, 50] \times [0, 50]$ is shown. The numbers in this figure correspond to the numbers of the activity types.

In the figure we see the following things. Type 7 and type 8 activity are seen for high values
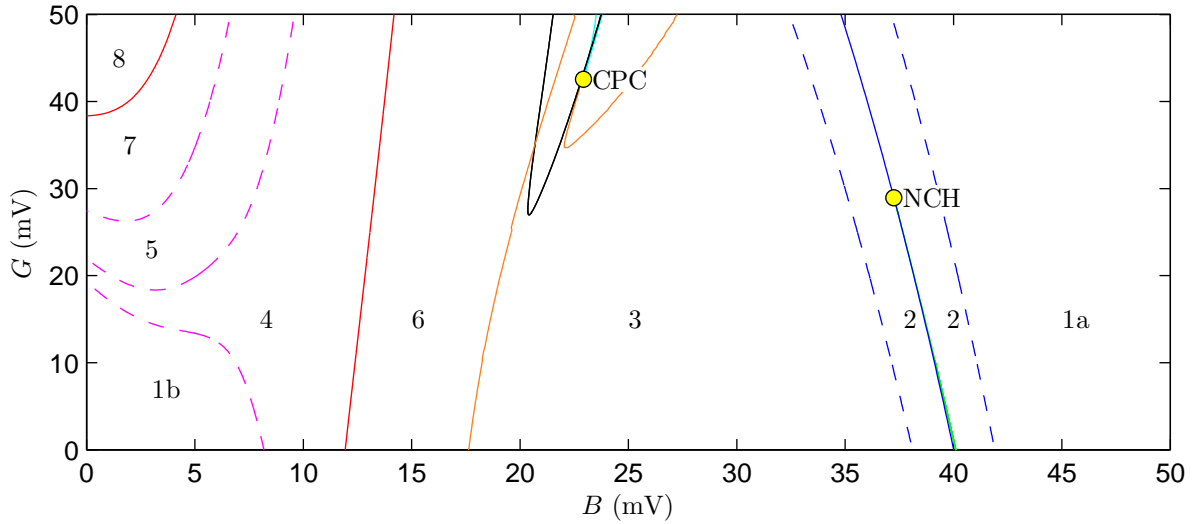
Figure 3.16: Plot of activity types found in B-G-plane. The solid blue line represent a curve of limit points. The dashed blue lines also represent curves of limit points but then for $I = 90 \pm 3\sigma$. The green line (almost on the blue line) is the curve of homoclinic bifurcations. Red lines indicate Hopf bifurcations. The black line is a period doubling curve. The cyan line indicate a limit point of cycle curve. The other colors indicate lines that are not bifurcations. The orange line indicates the curve of inflection points in the limit cycle. The magenta lines indicate a constant imaginary part of an eigenvalue.

of G and low values of B. For these values the slow inhibitory cells don't play a big role. The main inhibition of the system is done by the fast inhibitory cells. This causes the high frequencies seen for type 7 and 8. Type 7 activity has, besides with type 8, a boundary with type 5 activity. Type 5 activity borders to type 4 activity. For this type of activity the main inhibition comes from the slow inhibitory cells, this causes the noisy α-rhythm seen for this type of activity.

From type 4 activity we can go to type 1b activity. This is seen for low values of B and G. In this case there is nearly no inhibition. Therefore the potential of the pyramidal cells, u_{py}, is high for this case. Besides type 1b and type 5 activity type 4 has also a border with type 6 activity. This is the curve of Hopf bifurcations. Type 6 activity can be seen for mid values of B at all values of G. This is the result of the slow inhibition of the fast inhibitory cells. For mid values of B the fast inhibitory cells are inhibited so much by the slow inhibitory cells that also for high values of G they doesn't have much influence on the pyramidal cells.

As mentioned before we can pas from type 6 activity to type 3 activity if we cross the inflection point curve. If B is increased further we see first sporadic SWDs (type 2) and later type 1a activity. In the region with type 1a activity the inhibition is large compared to the excitation and the potential of the pyramidal cells is low.

For mid values of B and high values of G we see in figure 3.16 some other activity regions. The black curve represents a curve of period doublings. Inside this curve there lays a period doubling curve of the period doubled cycle (not shown in figure 3.16) and the system generates chaotic activity. A bit to the right a second curve of inflection points is shown. In this region the system has a stable limit cycle with two spikes followed by a wave, like we saw in the upper plot of figure 3.4.

Our activity map in figure 3.16 agrees for a large part with the colour map of Wendling et al. [28] (see figure 3.6). The main difference is that type 6 activity in our figure is seen for all values of G if B is at an intermediate value. In the map by Wendling this is only for lower values of G, for higher values of G they call this type 4 activity. We pointed at this difference before, it's probably a difference in the definition of the activity types.

In this section we showed an activity map for $(B, G) \in [0, 50] \times [0, 50]$. Some of the boundaries between the different activity types were formed by continuation of codim 1 points in two parameters. In order to understand how these codim 1 points are connected and from what codim 2 points they arise we will look in the next section at the continuation of these bifurcation for a broader parameter range.

3.6   Continuation of codim 1 bifurcations

In this section a codim 1 bifurcation diagram is presented for a much bigger region of parameters B and G. This can be found in figure 3.17. A large part of this region will correspond to physically unrealistic values, because B or G is negative or extremely large. However, some codim 2 points are found for these values. Some of these codim 2 points are starting points of codim 1 curves, like Bodagnov-Takens or zero-Hopf (fold-Hopf) points.

In figure 3.17 one can see that the two limit point curves of figure 3.16 are connected to each other via several cusp points and form a closed curve in the B-G-space. In the upper inset of figure 3.16 one can see that around $(B, G) = (15, 400)$ this curve crosses itself and there are two cusp points close to this point. In this way, a small region with a triangular shape is formed. In this region the system has five equilibria. Inside the rest of the region enclosed by the curve there are 3 equilibria.

Along the big limit point curve two zero-Hopf points are detected. At a zero-Hopf point a curve of Hopf bifurcations intersects tangential to the curve of limit points. The normal form coefficients provided by Matcont are $(s, \theta) \approx (-1, -0.96)$ for the zero-Hopf point around $B = 0$ and $(s, \theta) \approx (1, 1.96)$ for the zero-Hopf point around $B = 20$. Because for both points the coefficients s and θ have the same sign the zero-Hopf point has a relatively simple normal form: there don't start Neymarck-Sacker and homoclinic curves from this point [13].

It turns out that the two zero-Hopf points are connected by a closed curve of Hopf points. This curve of Hopf points is the one that generates the limit cycle with high frequency found in the bifurcation diagram for B in case $G = 50$. Along this curve of Hopf points two generalized Hopf (GH) points are found. At a generalized Hopf point the Hopf bifurcation turns from subcritical to supercritical and v.v. It's also the starting point for a limit point of cycle (LPC) curve. One can see that the two GH points on the fast Hopf curve are connected via a LPC curve.

The Hopf points, found in the bifurcation diagrams for B as the point from which the approximately 10Hz limit cycle starts, are part of a curve of Hopf points that start at the Bodagnov-Takens point at $(B, G) \approx (55, 1535)$. From this Bodagnov-Takens point also starts the curve of homoclinic bifurcations that causes the SWD cycle to disappear. The homoclinic curve sometimes falls together with a limit point forming a saddle-node on an invariant curve (SNIC). This homoclinic curve ends at the Bodagnov-Takens point around $B \approx 47$ and $G \approx -97$. The Hopf curve that starts from this Bodagnov-Takens point continues for values of G far below zero.

The Hopf curve that starts from the Bodagnov-Takens point at $(B, G) \approx (55, 1535)$ also has a generalized Hopf bifurcation at $(B, G) \approx (54, 1450)$. From this point starts a limit point of cycle curve. On this curve lay both limit point of cycles that are detected during the continuation in B for $G = 50$. Also the cusp point of cycles seen in figure 3.16 lays on this curve. This curve has another cusp point of cycles around $(B, G) \approx (41, 558)$. From there on the limit point of cycle curve walks close along the homoclinic bifurcation curve till it stops at the point marked 'NH' that lays on the homoclinic curve. The point 'NH' indicates a neutral homoclinic orbit, i.e. a point where the saddle quantity of the homoclinic orbit is zero [15].

Further we see from figure 3.17 that the two period doubling points found for continuation in B for $G = 50$ are connected with each other with a closed curve. Along this curve there were no codim 2 bifurcations detected. Inside the region enclosed by the period doubling curve there

lays a period doubling curve of the period doubled limit cycle, for clarity this curve is not shown in figure 3.17. In the region enclosed by the period doubling curve the system is chaotic and the system produces limit cycles with a complex wave shape.

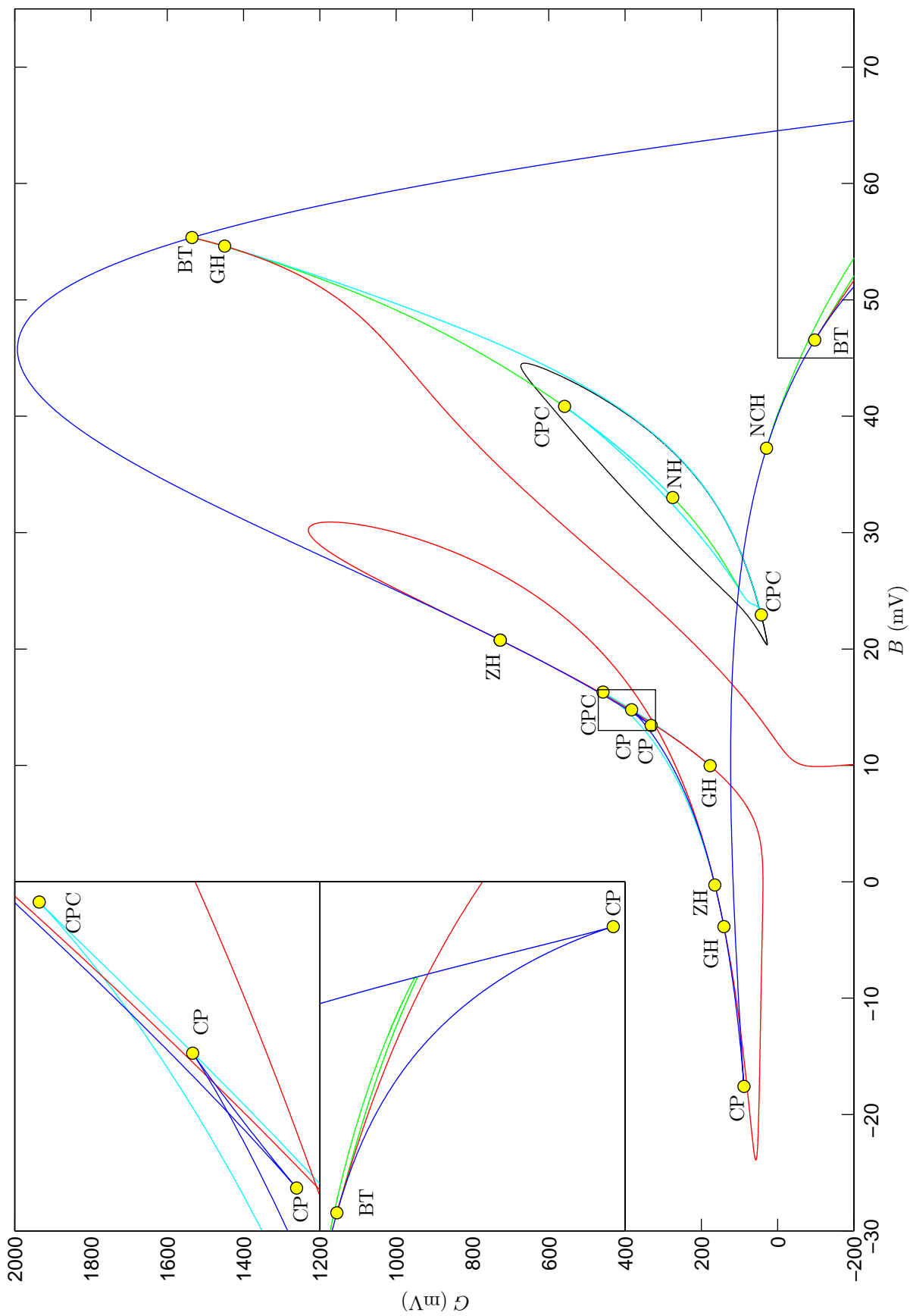Figure 3.17: Bifurcation plot of the *B*-*G*-plane. Blue: limit points. Red: Hopf. Green: homoclinic bifurcation. Cyan: limit point of cycles. Black: period doubling. Upper inset: enlargement of the middle box. Bottom inset: continuation of the figure at the lower right corner.

Chapter 4

Conclusion & discussion

In this report we gave an overview of neural mass models for cortical columns. After this we investigated the neural mass model by Wendling et al. [28] in more detail. A feature of the Wendling model is that it has two inhibitory populations. These two populations both give inhibitory feedback to the pyramidal cells but with a different timescale. Our main target was to find out what types of activity this model can generate and what the influence of inhibition on these activity types is.

We gave a description of different activity types that can be seen in the Wendling model. A part of these activity types was also described by Wendling et al. [28] and by Blenkinsop et al. [2]. We distinguished two new activity types. One is a γ-oscillation that is generated by a limit cycle. The other is noisy γ-activity that arises from noise-driven perturbations around an equilibrium.

Our description of the activity types was done in a more mathematical way then that of Wendling et al. [28]. In the description of the activity types we looked at the origin of the activity, i.e does the activity come from a limit cycle or from noisy perturbations around an equilibrium point.

After this we did bifurcation analysis and investigated the influence of the synaptic gain of the slow inhibitory PSP (B). It turned out that the bifurcations we found explain the transition between activities that are generated from a limit cycle and those that are generated from noisy perturbations around an equilibrium. The boundary between α-oscillations and noisy α-activity was formed by a Hopf bifurcation. This bifurcation gives a strict bound between these activities.

The bound between SWD and normal background activity was found to be a limit point bifurcation if no noise was added to the system. If the system receives a noisy input then there exist a transition region where sporadic SWD's were seen. As bounds for this transition region we proposed to use the limit point curves for a fixed input of $\mu \pm 3\sigma$, where μ is the mean of the input and σ is the standard deviation. This because the location of this limit point is very sensible for a change in input.

Our explanation for the sporadic spike activity is different from that given by Blenkinsop et al. [2]. They suggest that the sporadic spikes are a consequence of the fact that the period of a limit cycle goes to infinity if the limit cycle approaches a homoclinic bifurcation. Limit cycles close to a homoclinic bifurcation are for a relatively long time close to the equilibrium point of the homoclinic curve and are a relatively short time far away from it. Our explanation seems more logical, because it also explains the effect of the input noise strength which is related to the size of the sporadic spike region.

To find the other transitions between activity types we needed other criteria. Blenkinsop et al. found out that the transition between α-rhythm oscillations and SWD was a consequence of an inflection point in the limit cycle. This inflection point gives a strict boundary between these two activities. If this boundary is crossed one sees an immediate change in the dynamics of the system. It happens also in other models for neuronal activity that the transition between

α-oscillations and SWD is formed by an inflection point, for example in the thalamo-cortical model discussed by Breakspear et al. [4].

In [23] a method is proposed to continue these inflection points in two parameters. Unfortunately, we couldn't found an implementation of this method. Therefore we applied a work around to continue a curve of inflection points. A future task may be to make an implementation of this method in order to continue curves of inflection points in an easy way.

Further we wanted to find the transitions between activity types that are generated from noisy perturbations around an equilibrium. We found a reasonable bound for these activities by looking at the imaginary part of a complex conjugated pair of eigenvalues of the equilibrium point. The imaginary part of this eigenvalue divided by 2π gave approximately the frequency that had the highest power. We presented a way to continue curves with a constant imaginary part of this eigenvalue and used this to separate the equilibrium activity types.

The boundaries we choose for these equilibrium activity types correspond to a peak of 7, 13 and 25Hz in the frequency spectrum. These values were chosen by using the bounds of the frequency bands for α- and γ-activity found in literature. About the precise value of these bounds can be discussed. The bounds for the α- and γ-band in literature vary also. However, it turns out that the precise value doesn't matter because the bounds between these activity types are soft. One doesn't see an immediate change in activity but more a gradual change. Therefore one must see these borders more as a rough indication.

In the activity map we found for the synaptic gains of the two inhibitory PSPs we saw that slow inhibition has more influence then fast inhibition. The activity types that arises due to the slow inhibition (activity types with a frequency in the α range) are seen in large regions of the parameter space, including relatively high values of the fast synaptic gain. In contrast to the activity types that arise from purely the fast inhibitory PSP (activity types with a frequency in the γ range). These are seen only for high values of fast synaptic gain and low values of the slow synaptic gain. The reason for this is that the slow inhibitory cells project to the fast inhibitory cells and therefore inhibit the influence of the fast inhibitory PSP.

In the regions were both the fast and the slow inhibitory PSP play a role the system produces an activity type with a frequency in the range 13-25Hz. This activity has a relatively low amplitude. It can be compared with the fast onset activity seen at a seizure onset [28]. In the model this activity is a mixture of the two timescales. It's in fact the same phenomenon as described by David & Friston [5]. This activity type arises from noisy perturbations around an equilibrium. There is no equivalent activity type that is generated from a stable limit cycle with the same frequency. This in contrast to the α- and γ-activity that arises both as limit cycle activity and as equilibrium activity.

Another effect of the fast inhibitory process can be seen at high values of the fast synaptic gain and medium values of the slow one. In this region the model is able to produces pSWD with two or three spikes and other complex activities. These type of activities are also observed in the model by Goodfellow et al. [10] that also has two different inhibitory timescales, but not in the Jansen & Rit model that has only the slow one. According to [2] these activity types are commonly observed in EEGs of epilepsy patients.

We can conclude that although the fast inhibition doesn't have a large influence on the activity types it does play an important role. It is crucial in the generation of some epileptogenic activity types like fast onset activity and pSWD. Realistic NMMs that try to model types of epilepsy that features these activities, should therefore include a fast and slow inhibitory timescale.

In this report we investigated the activity of one single neural mass. However, in most neural mass models multiple cortical columns are coupled together. It is interesting to see if this produces other, more complex, types of activity and how this affects the activity map. Especially in cases were the cortical columns don't have the same parameters. In this way one has a heterogeneous network of cortical columns that comes closer to the reality.

Appendix A

Continuation of non-bifurcations

In this chapter is described how certain non-bifurcation points can be continued using bifurcation software like Matcont. Therefore we extend the system we investigate with some extra differential equations. First is described how eigenvalues of an equilibrium point can continued. Then a method is described that has a limit point if a linear combination of system variables has a certain value. We will combine these two principles to give extended systems that are able to continue the curves discussed in chapter 3.4.

In the whole chapter we will use that $\dot{x} = f(x, \alpha)$ denote the original system of differential equations, where $x \in \mathbb{R}^n$ represent the system variables and $\alpha \in \mathbb{R}^m$ the parameters. Further we define J to be the Jacobian of the original system:

$$J(x, \alpha) := \frac{\partial f(x, \alpha)}{\partial x}.$$

A.1   Continuation of eigenvalues

In this section we describe how a system of differential equations can extended in a way that the eigenvalues can continued as system variables. First we will treat this for a real eigenvalue and later for a complex conjugated pair of eigenvalues.

A.1.1   Continuation of a real eigenvalue

Let $\lambda \in \mathbb{R}$ be an eigenvalue of J and v a corresponding eigenvector. Then by definition it holds that:

$$Jv = \lambda v \quad \Longleftrightarrow \quad Jv - \lambda v = 0. \tag{A.1}$$

We can require v to have unit length:

$$<v, v> = 1 \quad \Longleftrightarrow \quad <v, v> - 1 = 0, \tag{A.2}$$

where $< \cdot, \cdot >$ denotes the standard innerproduct on $\mathbb{R}^n$.

We extend the original system of differential equations in the following way:

$$\dot{x} = f(x, \alpha), \tag{A.3a}$$

$$\dot{v} = Jv - \lambda v, \tag{A.3b}$$

$$\dot{\lambda} = <v, v> - 1. \tag{A.3c}$$

From the results in equations (A.1) and (A.2) it's clear that this system has an equilibrium point if x is an equilibrium point of the original system and v is an eigenvector with unit length to the eigenvalue λ of the linearization of this equilibrium.

We can continue an equilibrium of the extended system (A.3) in one parameter. However, it could be that the extra equations cause that the extended system gets additional limit points. It turns out that this is the case only if the multiplicity of the eigenvalue is greater then 1.

To prove this we compute the Jacobian of the extended system:

$$\begin{bmatrix} J & 0 & 0 \\ \frac{\partial(Jv)}{\partial x} & J - \lambda I & -v \\ 0 & 2v^T & 0 \end{bmatrix}.$$

This matrix is a block lower triangular matrix. We know that the extended system has a limit point if it's Jacobian has an eigenvalue 0. This is the case if J has a zero eigenvalue or the matrix

$$K := \begin{bmatrix} J - \lambda I & -v \\ 2v^T & 0 \end{bmatrix},$$

has a zero eigenvalue. The matrix J has a zero eigenvalue if the original system has a limit point.

We know that the matrix K has an eigenvalue 0 if we can find a vector $y \in \mathbb{R}^n$ and a scalar $\alpha \in \mathbb{R}$ such that $(y, \alpha) \neq 0$ and:

$$\begin{bmatrix} 0 \\ 0 \end{bmatrix} = K \begin{bmatrix} y \\ \alpha \end{bmatrix} = \begin{bmatrix} J - \lambda I & -v \\ 2v^T & 0 \end{bmatrix} \begin{bmatrix} y \\ \alpha \end{bmatrix} = \begin{bmatrix} (J - \lambda I)y - \alpha v \\ 2v^T y \end{bmatrix} \tag{A.4}$$

If we multiply the upper block with $(J - \lambda I)$ from the left it follows that:

$$0 = (J - \lambda I)^2 y - \alpha(J - \lambda I)v = (J - \lambda I)^2 y,$$

since $(J - \lambda I)v = 0$ because v is an eigenvector of J. So we find that

$$y \in \mathcal{N}(J - \lambda I)^2,$$

where $\mathcal{N}(J - \lambda I)^2$ denotes the nullspace of $(J - \lambda I)^2$.

In case λ is a simple eigenvalue of J (λ is an eigenvalue with algebraic multiplicity one), it follows from generalized eigenvalue theory that $\mathcal{N}(J - \lambda I) = \mathcal{N}(J - \lambda I)^2$. Since v is an eigenvalue of J we know that $v \neq 0$ and $v \in \mathcal{N}(J - \lambda I)$. From the assumption that λ is a simple eigenvalue it follows that $\dim(\mathcal{N}(J - \lambda I)) = 1$. So v spans $\mathcal{N}(J - \lambda I)$. Therefore $y = \gamma v$ for some $\gamma \in \mathbb{R}$. From the bottom entries in equation (A.4) it follows that:

$$0 = 2v^T y = 2\gamma v^T v = 2\gamma \quad \Longrightarrow \quad \gamma = 0 \quad \Longrightarrow \quad y = 0,$$

where we used that $v^T v = <v, v> = 1$. So $y = 0$. From the upper entries in equation (A.4) we find:

$$0 = (J - \lambda I)y - \alpha v = -\alpha v.$$

Since $v \neq 0$, it's an eigenvector, we must have $\alpha = 0$. It follows that the $(y, \alpha) = 0$ and therefore the matrix K doesn't have an eigenvalue 0. This means that as long as the matrix J has a simple eigenvalue the extended system don't have additional limit points.

In case λ is not a simple eigenvalue of J then we can distinct two sub cases. In the first sub case $\dim(\mathcal{N}(J - \lambda I)) \geq 2$. Then we can find a y such that $<y, v> = 0$ and y an eigenvector of J. It's easy to see that $(y, 0)$ in this case is a non trivial solution of (A.4). So K has a eigenvalue 0.

In the second sub case the matrix doesn't have a full eigenspace. We have

$$\dim(\mathcal{N}(J - \lambda I)) = 1.$$

In this case it's known that there exist a y such that $<v, y> = 0$ and $(J - \lambda I)y = v$. In this case $(y, 1)$ is a non-trivial solution of (A.4). It follows that 0 is an eigenvalue of K in this case.

So we showed that the extended system (A.3) can continue a real eigenvalue of the original system. The extended system (A.3) has limit points if the original system has a limit point or if the eigenvalue that is continued is non-simple. The latter is generally the case if two real eigenvalues fall together and form a pair of complex conjugated eigenvalues.

A.1.2 Continuation of a complex conjugated pair of eigenvalues

Now we focus on continuing a complex conjugated pair of eigenvalues. Let $\mu + i\theta$ be a complex eigenvalue of J where $\mu \in \mathbb{R}$ and $\theta \in \mathbb{R}_{\geq 0}$. Denote the corresponding eigenvector by $p + iq$ with $p, q \in \mathbb{R}^n$. Then by definition it holds that:

$$J(p + iq) = (\mu + i\theta)(p + iq) = (\mu p - \theta q) + i(\theta p + \mu q).$$

Splitting the real and imaginary part gives:

$$0 = Jp - \mu p + \theta q, \tag{A.5a}$$
$$0 = Jq - \theta p - \mu q. \tag{A.5b}$$

Like in the real case we can require that the eigenvector $p + iq$ has unit length. In terms of the innerproduct on $\mathbb{R}^n$ this gives.

$$0 = <p, p> + <q, q> -1, \tag{A.6}$$

In the complex case we have an addition degree of freedom. Therefore we can require that:

$$0 = <p, q> . \tag{A.7}$$

In the complex case we extend the original system of differential equations to the following system of $3n + 2$ equations:

$$\dot{x} = f(x, \alpha), \tag{A.8a}$$
$$\dot{p} = Jp - \mu p + \theta q, \tag{A.8b}$$
$$\dot{q} = Jq - \theta p - \mu q, \tag{A.8c}$$
$$\dot{\mu} = <p, p> + <q, q> -1, \tag{A.8d}$$
$$\dot{\theta} = <p, q> . \tag{A.8e}$$

From the results in equations (A.5), (A.6) and (A.7) it's clear that this system has an equilibrium point if x is an equilibrium point of the original system and $p + iq$ is an eigenvector to the eigenvalue $\mu + i\theta$ of the linearization of this equilibrium.

A.2 Limit point at certain value of system variables

In this section is explained how a curve can continued at which a linear combination of the system variable has a certain value. So we want to find a curve in a two parameter space where $<w, x> = c$ for some vector $w \in \mathbb{R}^n$ and $c \in \mathbb{R}$. In order to do this we extend the system with an auxiliary variable $h \in \mathbb{R}$ in the following way:

$$\dot{x} = f(x, \alpha), \tag{A.9a}$$
$$\dot{h} = <w, x> -h^2 - c. \tag{A.9b}$$

It can seen that this extended system has an equilibrium if x is an equilibrium of the original system and $h = \pm\sqrt{<w, x> -c}$. It follows that h is real in case $<w, x> -c \geq 0$. So this extended system doesn't have a real equilibrium everywhere the original system has an equilibrium.

Further the extended system in (A.9) has a limit point at $< w, x >= c$. To prove this we compute the Jacobian of this extended system. This gives:

$$\begin{bmatrix} J & 0 \\ w^T & 2h \end{bmatrix}.$$

We see that the Jacobian of the extended system is again lower triangular. Therefore the eigenvalues are given by those of J and the scalar $2h$. The first one causes that the extended system has a limit point if the original system has a limit point. The scalar $2h$ gives a limit point if $h = 0$. Since we know that h at an equilibrium point is given by $h = \pm\sqrt{< w, x > -c}$ it follows that $h = 0$ if and only if $< w, x >= c$. So the auxiliary variable h gives a limit point if and only if $< w, x >= c$.

The extended system in equation (A.9) can be used to start an equilibrium continuation from a point in a two parameter space where $< w, x >\geq c$. This equilibrium can continued until a limit point induced by the auxiliary variable h is reached. This is easy to see since $h = 0$ in this case. The obtained limit point can continued in two parameters and gives a curve where $< w, x >= c$.

A.3 Continuation of possible boundaries of activity types

In the previous two sections different extensions of a system of differential equations are discussed. In this section is showed how these extensions can be used in order to continue the boundaries of activity types as discussed in chapter 3.4. We start with the boundaries used by Blenkinsop et al. [2]. After this the extended system, that is used to continue the boundaries where the imaginary part of a complex eigenvalue is fixed, is given.

A.3.1 Transition of leading eigenvalue

To distinguish the different activity types in the Wendling model Blenkinshop et al. [2] proposed to use the curve that is the transition between a real and complex leading eigenvalue as boundary. This transition can take place in two ways. Case 1: the system has two real eigenvalue that collide and form a complex pair. In this case the system has a double real eigenvalue at the boundary. Case 2: the system has a real eigenvalue, say λ, and a complex conjugated eigenvalue pair, say $\mu + i\theta$. Due variation of the parameters μ can get bigger then λ. At the boundary we have in this case $\lambda = \mu$.

To find these boundaries by numerical continuation we use the methods described in the sections before. To find the place where the system has a double leading real eigenvalue we need to continue the real eigenvalue that is leading. This can we do by extending the original systems as described in equation (A.3) and continue the leading real eigenvalue. From section A.1.1 we know that this system has a limit point in case the system has a double reel eigenvalue. One can continue this limit point in two variable two obtain a curve where the system has a double leading eigenvalue.

For case 2 we need to continue also a complex conjugated pair of eigenvalues. Therefore we extend our system with both equations from (A.3) and (A.8). We want that the system has a limit point if the real eigenvalue is as big as the real part of the complex eigenvalue, so $\lambda - \mu = 0$. To do this we extend this extended system with the method described in section A.2.

All together we get the following big system:

$$\dot{x} = f(x, \alpha), \tag{A.10a}$$

$$\dot{v} = Jv - \lambda v, \tag{A.10b}$$

$$\dot{\lambda} = <v, v> -1, \tag{A.10c}$$

$$\dot{p} = Jp - \mu p + \theta q, \tag{A.10d}$$

$$\dot{q} = Jq - \theta p - \mu q, \tag{A.10e}$$

$$\dot{\mu} = <p, p> + <q, q> -1, \tag{A.10f}$$

$$\dot{\theta} = <p, q>, \tag{A.10g}$$

$$\dot{h} = (\lambda - \mu) - h^2. \tag{A.10h}$$

This big system has an equilibrium in the region where $\lambda \geq \mu$ and has limit points in case the system has a double real eigenvalue and in case the real part of the complex eigenvalue becomes larger then the real eigenvalue.

This system must be initialized at an equilibrium point of the original system. The leading real eigenvalue, it's corresponding eigenvector and the complex eigenvalue of which the real part becomes larger then the leading real eigenvalue and it's eigenvector must also be filled in as initial conditions.

A.3.2 Continuation of eigenvalues with a fixed imaginary part

For the boundaries between equilibrium activity types we wanted to find curves where the imaginary part of a complex eigenvalue is fixed at some value. In order to do this we extend the system as described in section A.1.2 to continue a complex eigenvalue. This extended system we extend again by the method described in section A.2. We obtained the following system:

$$\dot{x} = f(x, \alpha), \tag{A.11a}$$

$$\dot{p} = Jp - \mu p + \theta q, \tag{A.11b}$$

$$\dot{q} = Jq - \theta p - \mu q, \tag{A.11c}$$

$$\dot{\mu} = <p, p> + <q, q> -1, \tag{A.11d}$$

$$\dot{\theta} = <p, q>, \tag{A.11e}$$

$$\dot{h} = -\theta - h^2 + c. \tag{A.11f}$$

This extended system has a limit point in case the imaginary part of the eigenvalue θ equals the desired imaginary part c. It must be initialized in a region where $c \geq \theta$ and then continued in one parameter till a limit point induced by the auxiliary variable h is reached. The obtained limit point can be continued in two parameters to obtain a curve in the parameter space.

Appendix B

Simulation source code

In this appendix our implementation for the Wendling model is given. This implementation is written in Matlab and uses the Milstein method to solve the stochastic differential equations in equation (3.1) numerically. The source code contains some comments that explain the different variables and the algorithm.

```matlab
1   tic; %To measure computation time
2   %% Simulation settings
3   Npart=2;                      %Number of parts for fourier transform including intial
                 part
4   Tend=10*Npart;               %Total simulation time
5   NTST=Tend*10000;             %Number of Time Steps
6   Nout=5;                      %Output every 5th timestep
7
8   deltat=Tend/NTST;            %Timestep size
9
10  %% Parameter settings
11  A=5;                         %Average excitory synaptic gain
12  B=25;                        %Average slow inhibitory synaptic gain
13  G=15;                        %Average fast inhibitory synaptic gain
14
15  a=100;                       %Inverse of excitory time constant
16  b=50;                        %Inverse of slow inhibitory time constant
17  g=500;                       %Inverse of fast inhibitory time constant
18
19  C=135;                       %Connectivity parameter
20  C1=C;
21  C2=0.8*C;
22  C3=0.25*C;
23  C4=0.25*C;
24  C5=0.3*C;
25  C6=0.1*C;
26  C7=0.8*C;
27
28  pf=90;                       %Mean input
29  sd=2;                        %Standard deviation input
30
31  %% Initial condititons
32  x=zeros(4,1);
33  y=zeros(4,1);
34
35  %% Initialise variables for computation
36   Im=eye(4,4);
37
38  Q1=-deltat*diag([a^2,a^2,b^2,g^2]);
39  Q2=Im-2*deltat*diag([a,a,b,g]);
40  Q3=deltat*diag([A*a,A*a,B*b,G*g]);
41
```

```matlab
42   fd=[0;A*a*pf/C2;0;0]*deltat;
43   fs=[0;A*a/C2;0;0]*sqrt(deltat)*sd*randn(1,NTST);
44
45   P=[[0, C2, -C4,-C7];
46       [C1,0,0,0];
47       [C3,0,0,0];
48       [C5,0,-C6,0]];
49
50   u=P*x;
51   uout=zeros(4,ceil(NTST/Nout)+1);
52   uout(:,1)=u;
53
54   xn=zeros(4,1);
55   yn=zeros(4,1);
56
57   %%
58   t1=toc;
59   disp(['Initialisation time: ',num2str(t1)]);
60   disp('Start simulation');
61
62   tel=0;
63   indexplot=2;
64   for i=1:NTST
65       xn=x+deltat*y;
66       yn=Q1*x+Q2*y+Q3*sigm(u)+fd+fs(:,i);
67
68       x=xn;
69       y=yn;
70       u=P*x;
71
72       %Saves u for output every Nout iterations
73       tel=tel+1;
74       if tel==Nout
75           tel=0;
76           uout(:,indexplot)=u;
77           indexplot=indexplot+1;
78       end
79   end
80
81   t2=toc;
82   disp(['Simulation complete, duration: ',num2str(t2-t1)]);
83
84   %% Post processing
85
86   %Plot time series
87   figure;
88   plot(0:deltat*Nout:Tend,uout(1,:));
89   xlim([0 Tend])
90   set(gca,'YDir','reverse');
91
92   %Calculate frequency spectrum
93   for j=1:Npart-1;
94       [f,pow]=freqplot(uout(1,floor(NTST*j/(Npart*Nout)):floor(NTST*(j+1)/(Npart*
               Nout)))-mean(uout(1,floor(NTST*j/(Npart*Nout)):floor(NTST*(j+1)/(Npart*
               Nout)))),1/(deltat*Nout));
95       if j>1;
96           powtot=powtot+pow;
97       else
98           powtot=pow;
99       end
100  end
101
102  %Display frequency spectrum
```

```matlab
103    figure;
104    plot(f, powtot/(Npart-1));
105    xlim([0  50])
106
107    toc;                        %Displays total computation time
```

Bibliography

[1] B. S. Bhattacharya, D. Coyle, and L. P. Maguire. A thalamo-cortico-thalamic neural mass model to study alpha rhythms in alzheimer's disease. *Neural Networks*, 24(6):631–645, 2011.

[2] A. Blenkinsop, A. Valentin, M. P. Richardson, and J. R. Terry. The dynamic evolution of focal-onset epilepsies - combining theoretical and clinical observations. *European Journal of Neuroscience*, 36(2):2188–2200, 2012.

[3] A. Bragin, J. Engel Jr., C. L. Wilson, I. Fried, and G. W. Mathern. Hippocampal and entorhinal cortex high-frequency oscillations (100-500 hz) in human epileptic brain and in kainic acid-treated rats with chronic seizures. *Epilepsia*, 40(2):127–137, 1999.

[4] M. Breakspear, J. A. Roberts, J. R. Terry, S. Rodrigues, N. Mahant, and P. A. Robinson. A unifying explanation of primary generalized seizures through nonlinear brain modeling and bifurcation analysis. *Cerebral Cortex*, 16(9):1296–1313, 2006.

[5] O. David and K. J. Friston. A neural mass model for meg/eeg: Coupling and neuronal dynamics. *NeuroImage*, 20(3):1743–1755, 2003.

[6] O. David, L. Harrison, and K. J. Friston. Modelling event-related responses in the brain. *NeuroImage*, 25(3):756–770, 2005.

[7] G. Deco, V. K. Jirsa, P. A. Robinson, M. Breakspear, and K. Friston. The dynamic brain: From spiking neurons to neural masses and cortical fields. *PLoS Computational Biology*, 4(8), 2008.

[8] A. Dhooge, W. Govaerts, and Yu A. Kuznetsov. Matcont: A matlab package for numerical bifurcation analysis of odes. *ACM Transactions on Mathematical Software*, 29(2):141–164, 2003.

[9] WJ Freeman. Models of the dynamics of neural populations. *Electroencephalography and clinical neurophysiology. Supplement*, (34):9–18, 1977.

[10] M. Goodfellow, K. Schindler, and G. Baier. Intermittent spike-wave dynamics in a heterogeneous, spatially extended neural mass model. *NeuroImage*, 55(3):920–932, 2011.

[11] M. Goodfellow, K. Schindler, and G. Baier. Self-organised transients in a neural mass model of epileptogenic tissue dynamics. *NeuroImage*, 59(3):2644–2660, 2012.

[12] F. Grimbert and O. Faugeras. Bifurcation analysis of jansen's neural mass model. *Neural computation*, 18(12):3052–3068, 2006.

[13] J. Guckenheimer and Y. A. Kuznetsov. Fold-Hopf bifurcation. *Scholarpedia*, 2(10):1855, 2007. revision 91277.

[14] R. Hindriks and M. J. A. M. van Putten. Meanfield modeling of propofol-induced changes in spontaneous eeg rhythms. *NeuroImage*, 60(4):2323–2334, 2012.

[15] A. J. Homburg and B. Sandstede. *Homoclinic and heteroclinic bifurcations in vector fields*, volume 3 of *Handbook of Dynamical Systems*. 2010.

[16] J. R. Hughes. Gamma, fast, and ultrafast waves of the brain: Their relationships with epilepsy and behavior. *Epilepsy and Behavior*, 13(1), 2008.

[17] B. H. Jansen and V. G. Rit. Electroencephalogram and visual evoked potential generation in a mathematical model of coupled cortical columns. *Biological cybernetics*, 73(4):357–366, 1995.

[18] B. H. Jansen, G. Zouridakis, and M. E. Brandt. A neurophysiologically-based mathematical model of flash visual evoked potentials. *Biological cybernetics*, 68(3):275–283, 1993.

[19] Y.A. Kuznetsov. *Elements of Applied Bifurcation Theory*. Springer, 3th edition, 2004.

[20] F. H. Lopes da Silva, A. Hoeks, H. Smits, and L. H. Zetterberg. Model of brain rhythmic activity. the alpha rhythm of the thalamus. *Kybernetik*, 15(1):27–37, 1974.

[21] F. H. Lopes da Silva, A. van Rotterdam, P. Barts, E. van Heusden, and W. Burr. *Models of Neuronal Populations: The Basic Mechanisms of Rhythmicity*, volume 45 of *Progress in Brain Research*. 1976.

[22] PL Nunez. *Electric fields of the brain, 1981.* Oxford University Press, New York, 1981.

[23] S. Rodrigues, D. Barton, F. Marten, M. Kibuuka, G. Alarcon, M. P. Richardson, and J. R. Terry. A method for detecting false bifurcations in dynamical systems: Application to neural-field models. *Biological cybernetics*, 102(2):145–154, 2010.

[24] R. C. Sotero, N. J. Trujillo-Barreto, Y. Iturria-Medina, F. Carbonell, and J. C. Jimenez. Realistically coupled neural mass models can generate EEG rhythms. *Neural computation*, 19(2):478–512, 2007.

[25] Cornelis J Stam. *Nonlinear brain dynamics.* Nova Publishers, 2006.

[26] J. Touboul, F. Wendling, P. Chauvel, and O. Faugeras. Neural mass activity, bifurcations, and epilepsy. *Neural computation*, 23(12):3232–3286, 2011.

[27] A. van Rotterdam, F. H. Lopes da Silva, J. van den Ende, M. A. Viergever, and A. J. Hermans. A model of the spatial-temporal characteristics of the alpha rhythm. *Bulletin of mathematical biology*, 44(2):283–305, 1982.

[28] F. Wendling, F. Bartolomei, J. J. Bellanger, and P. Chauvel. Epileptic fast activity can be explained by a model of impaired gabaergic dendritic inhibition. *European Journal of Neuroscience*, 15(9):1499–1508, 2002.

[29] F. Wendling, F. Bartolomei, F. Mina, C. Huneau, and P. Benquet. Interictal spikes, fast ripples and seizures in partial epilepsies - combining multi-level computational models with experimental data. *European Journal of Neuroscience*, 36(2):2164–2177, 2012.

[30] F. Wendling, J. J. Bellanger, F. Bartolomei, and P. Chauvel. Relevance of nonlinear lumped-parameter models in the analysis of depth-eeg epileptic signals. *Biological cybernetics*, 83(4):367–378, 2000.

[31] F. Wendling, A. Hernandez, J. . Bellanger, P. Chauvel, and F. Bartolomei. Interictal to ictal transition in human temporal lobe epilepsy: Insights from a computational model of intracerebral EEG. *Journal of Clinical Neurophysiology*, 22(5):343–356, 2005.